

Stabilized finite element method for incompressible flows with high Reynolds number

E. Hachem*, B. Rivaux, T. Kloczko, H. Digonnet, T. Coupez

MINES ParisTech, Center for Materials Forming (CEMEF), UMR CNRS 7635, BP 207, 06904 Sophia-Antipolis, France

ARTICLE INFO

Article history:

Received 22 December 2009

Received in revised form 25 July 2010

Accepted 27 July 2010

Available online 4 August 2010

Keywords:

Stabilized FEM

VMS

High Reynolds number

2D & 3D lid-driven cavity

Backward-facing step

ABSTRACT

In the following paper, we discuss the exhaustive use and implementation of stabilization finite element methods for the resolution of the 3D time-dependent incompressible Navier–Stokes equations. The proposed method starts by the use of a finite element variational multiscale (VMS) method, which consists in here of a decomposition for both the velocity and the pressure fields into coarse/resolved scales and fine/unresolved scales. This choice of decomposition is shown to be favorable for simulating flows at high Reynolds number. We explore the behaviour and accuracy of the proposed approximation on three test cases. First, the lid-driven square cavity at Reynolds number up to 50,000 is compared with the highly resolved numerical simulations and second, the lid-driven cubic cavity up to $Re = 12,000$ is compared with the experimental data. Finally, we study the flow over a 2D backward-facing step at $Re = 42,000$. Results show that the present implementation is able to exhibit good stability and accuracy properties for high Reynolds number flows with unstructured meshes.

© 2010 Elsevier Inc. All rights reserved.

1. Introduction

The incompressible Navier–Stokes equations are used to model a number of important physical phenomena, including pipe flow, flow around airfoils, weather, blood flow and convective heat transfer inside industrial furnaces. Significant emphasis has been placed in the literature on developing stabilized formulations robust enough to model complex flows at high Reynolds number [1–4].

It is known that the Galerkin approximation of the Navier–Stokes equations may fail because of two reasons. Firstly, in convection dominated flows, for which layers appears where the velocity solution and its gradient exhibit rapid variation, the classical Galerkin approach leads to numerical oscillations in these layer regions which can spread quickly and pollute the entire solution domain. Secondly, the use of inappropriate combinations of interpolation functions to represent the velocity and pressure fields [5,6] yields unstable schemes. The pressure and convective instabilities associated with the Galerkin formulation are usually circumvented by addition of stabilization terms.

The present work aims at retaining the advantages of using linear approximations (P1 finite elements) regarding the accuracy and the computational cost, especially for 3D real applications. The use of unstructured meshes and thus automatic and adaptive mesh generation can be easily applicable. But it is well known that the combination of P1–P1 approximation for the velocity and the pressure does not lead to a stable discretization since it does not satisfy the Babuska–Brezzi condition.

Many measures may be distinguished to solve and get around these two difficulties, the instabilities in convection-dominated regime and the velocity–pressure compatibility condition. A very popular method was firstly proposed by Arnold, Brezzi and Fortin [7] for the Stokes problem. It was suggested to enrich the functional spaces with space of bubble functions

* Corresponding author. Tel.: +33 0 4 92 95 74 58; fax: +33 0 4 92 38 97 52.

E-mail address: Elie.Hachem@mines-paristech.fr (E. Hachem).

known as Mini-element. Since the bubble functions vanish on each element boundary, they can be eliminated and statically condensed giving rise to a stabilized formulation for equal-order linear element. In diffusion dominant cases, the Mini-element formulation of the problem yields acceptable results. However, when the convection terms dominate, the results can be impaired and an extension for this method is needed. Later, in [8], it was pointed out that resorting to these local bubbles is equivalent to using residual-based stabilized schemes with a natural way of choosing the stabilization parameters: the selection of the optimal bubble function reproducing the appropriate choice of the stability parameter. Thus, it is clear that the bubble can take different shapes for the diffusive dominated regime and for the advection-dominated flow regime. For example, it was shown in [9,10] that upwind bubbles could be used to reproduce the SUPG stabilization.

A standard reference for mixed finite element methods is the book of Brezzi and Fortin [11]. A brief history on residual based stabilisation methods can be found in Brezzi et al. [12], the book of Donea and Huerta [13], all the articles by Hughes et al. [14–16] on multiscale methods and SUPG/PSPG methods by Tezduyar [17]. The Unusual Stabilised finite element method (USFEM) was introduced by Franca and Farhat in [18]. Codina and co-workers introduced lately recent developments of residual based stabilisation methods using orthogonal subscales and time dependent subscales [19–23]. These methods are very promising and can be regarded as an open door to turbulence. At the same level, one can find a complete description on the use of variational multiscale method for turbulent flows in [24–26] where a three scale separation method was developed and applied.

In the past three decades, various numerical methods were developed to solve this problem [9,27–29]. The present work is inspired notably from [5,30] where only the enrichment of the velocity was considered, and from the work in [31] where the decomposition of the pressure was considered but tested for only laminar flow situations. In this sense, the main contributions of this work, considered as a continuation of those references, are a systematic use of the variational multiscale method [32–34] for three-dimensional problems and an implementation of a consistent formulation suitable for large problems with high Reynolds number and unstructured meshes. It resides in the combination of different published arguments, such as the use of the decomposition for both the velocity and the pressure fields into coarse scales and fine scales, the use of upwind bubble for the convection term in the fine scale equation, and finally, from an implementation point of view, the use of a matrix formulation needed simply for a direct static condensation. Consequently, a particular emphasis is placed on the performance of the implemented method for two-dimensional and three-dimensional problems with high Reynolds number, up to 50,000 and 12,000 respectively.

The outline of the paper is as follows: first, we present the time-dependent, three-dimensional, Navier–Stokes problem. In Section 3, we present the stabilizing schemes from a variational multiscale point of view to deal with convection dominated problems. In Section 4, the numerical performance of the presented method is demonstrated by means of 2D and 3D test cases. Comparisons with the literature results are presented. Finally, conclusions and perspectives are outlined.

2. The incompressible Navier–Stokes equations

Let $\Omega \subset \mathbb{R}^n$ be the spatial domain at time $t \in [0, T]$, where n is the number of space dimensions. Let Γ denote the boundary of Ω . We consider the following velocity–pressure formulation of the Navier–Stokes equations governing unsteady incompressible flows:

$$\rho(\partial_t \mathbf{u} + \mathbf{u} \cdot \nabla \mathbf{u}) - \nabla \cdot \boldsymbol{\sigma} = \mathbf{f} \quad \text{in } \Omega \times [0, T] \quad (1)$$

$$\nabla \cdot \mathbf{u} = 0 \quad \text{in } \Omega \times [0, T] \quad (2)$$

where ρ and \mathbf{u} are the density and the velocity, \mathbf{f} the body force vector per unity density and $\boldsymbol{\sigma}$ the stress tensor which reads:

$$\boldsymbol{\sigma} = 2\mu \boldsymbol{\varepsilon}(\mathbf{u}) - p \mathbf{I}_d \quad (3)$$

with p and μ the pressure and the dynamic viscosity, \mathbf{I}_d the identity tensor and $\boldsymbol{\varepsilon}$ the strain-rate tensor defined as

$$\boldsymbol{\varepsilon}(\mathbf{u}) = \frac{1}{2}(\nabla \mathbf{u} + {}^t \nabla \mathbf{u}) \quad (4)$$

Essential and natural boundary conditions for Eq. (1) are:

$$\mathbf{u} = \mathbf{g} \quad \text{on } \Gamma_g \times [0, T] \quad (5)$$

$$\mathbf{n} \cdot \boldsymbol{\sigma} = \mathbf{h} \quad \text{on } \Gamma_h \times [0, T] \quad (6)$$

Γ_g and Γ_h are complementary subsets of the domain boundary Γ . Functions \mathbf{g} and \mathbf{h} are given and \mathbf{n} is the unit outward normal vector of Γ . As initial condition, a divergence-free velocity field $\mathbf{u}_0(\mathbf{x})$ is specified over the domain Ω_t at $t = 0$:

$$\mathbf{u}(\mathbf{x}, 0) = \mathbf{u}_0(\mathbf{x}) \quad (7)$$

3. Multiscale variational approach

3.1. Weak formulation of the incompressible Navier–Stokes equations

The function space for the velocity and the scalar function space for the pressure are respectively defined by:

$$V = \{\mathbf{u}(\mathbf{x}, t) | \mathbf{u}(\mathbf{x}, t) \in H^1(\Omega)^n, \quad \mathbf{u} = \mathbf{g} \text{ on } \Gamma_g\} \quad (8)$$

$$Q = \{p(\mathbf{x}, t) | p(\mathbf{x}, t) \in L^2(\Omega)\} \quad (9)$$

and the weighting function space for the velocity

$$V_0 = \left\{ \mathbf{u}(\mathbf{x}, t) | \mathbf{u}(\mathbf{x}, t) \in H^1(\Omega)^n, \quad \mathbf{u} = \mathbf{0} \text{ on } \Gamma_g \right\} \quad (10)$$

The weak form of the system (1), (2) consists in finding $\mathbf{u} : [0, T] \rightarrow V, p : (0, T] \rightarrow Q$ such that:

$$\begin{cases} \rho(\partial_t \mathbf{u}, \mathbf{w})_\Omega + \rho(\mathbf{u} \cdot \nabla \mathbf{u}, \mathbf{w})_\Omega + (\boldsymbol{\sigma}(p, \mathbf{u}), \boldsymbol{\varepsilon}(\mathbf{w}))_\Omega = (\mathbf{f}, \mathbf{w})_\Omega + (\mathbf{h}, \mathbf{w})_{\Gamma_h} & \forall \mathbf{w} \in V_0 \\ (\nabla \cdot \mathbf{u}, q)_\Omega = 0 & \forall q \in Q \end{cases} \quad (11)$$

$$\begin{cases} (\nabla \cdot \mathbf{u}, q)_\Omega = 0 & \forall q \in Q \end{cases} \quad (12)$$

where $(\varphi, \psi)_\Omega = \int_\Omega \varphi \psi d\Omega$ is the standard scalar product in $L^2(\Omega)$. The standard Galerkin approximation consists in decomposing the domain Ω into N_{el} elements K such that they cover the domain and there are either disjoint or share a complete edge (or face in 3D). Using this partition \mathcal{T}_h , the above-defined functional spaces (10) and (9) are approached by finite dimensional spaces spanned by continuous piecewise polynomials such that:

$$V_h = \left\{ \mathbf{u}_h | \mathbf{u}_h \in C^0(\Omega)^n, \quad \mathbf{u}_{h|K} \in P^1(K)^n, \quad \forall K \in \mathcal{T}_h \right\} \quad (13)$$

$$Q_h = \left\{ p_h | p_h \in C^0(\Omega), \quad p_{h|K} \in P^1(K), \quad \forall K \in \mathcal{T}_h \right\} \quad (14)$$

The Galerkin discrete problem consists therefore in solving the following mixed problem:

Find a pair $\mathbf{u}_h : [0, T] \rightarrow V_h$ and $p_h : (0, T] \rightarrow Q_h$, such that: $\forall (\mathbf{w}_h, q_h) \in V_{h,0} \times Q_h$

$$\begin{cases} \rho(\partial_t \mathbf{u}_h, \mathbf{w}_h)_\Omega + \rho(\mathbf{u}_h \cdot \nabla \mathbf{u}_h, \mathbf{w}_h)_\Omega + (2\mu \boldsymbol{\varepsilon}(\mathbf{u}_h) : \boldsymbol{\varepsilon}(\mathbf{w}_h))_\Omega - (p_h, \nabla \cdot \mathbf{w}_h)_\Omega = (\mathbf{f}, \mathbf{w}_h)_\Omega + (\mathbf{h}, \mathbf{w}_h)_{\Gamma_h} \\ (\nabla \cdot \mathbf{u}_h, q_h)_\Omega = 0 \end{cases} \quad (15)$$

It is known that the finite element approximation (15) may fail because of two reasons: the inf-sup condition (Brezzi–Babuška) which required an appropriate pair of the function spaces for the velocity and the pressure. The second one is the dominance of the convective term which can generate spurious oscillations that will pollute the whole numerical solution. In the next section the general equations of time-dependent Navier–Stokes equation are solved. The stabilizing schemes from a variational multiscale point of view are described and presented. Both the velocity and the pressure spaces are enriched by a space of bubbles that cures the spurious oscillations in the convection-dominated regime as well as the pressure instability.

3.2. Basic principles of the multiscale approach

Following [28], we consider an overlapping sum decomposition of the velocity and the pressure fields into resolvable coarse-scale and unresolved fine-scale $\mathbf{u} = \mathbf{u}_h + \mathbf{u}'$ and $p = p_h + p'$. Likewise, we regard the same decomposition for the weighting functions $\mathbf{w} = \mathbf{w}_h + \mathbf{w}'$ and $q = q_h + q'$. The unresolved fine-scales are usually modelled using residual based terms that are derived consistently. The static condensation consists in substituting the fine-scale solution into the large-scale problem providing additional terms, tuned by a local time-dependent stabilizing parameter, that enhance the stability and accuracy of the standard Galerkin formulation for the transient non-linear Navier–Stokes equations. In order to represent these fine-scales, different bubble functions (similar to the Mini-element) may be used. The selection of the optimal bubble function reproduces the appropriate choice of the stability parameter [8,9].

The enrichment of the functional spaces is performed as follows: $V = V_h \oplus V'$, $V_0 = V_{h,0} \oplus V'_0$ and $Q = Q_h \oplus Q'$. Thus, the mixed-finite element approximation of problem (15) can read:

Find a pair $\mathbf{u} : [0, T] \rightarrow V$ and $p : (0, T] \rightarrow Q$ such that: $\forall (\mathbf{w}, q) \in V_0 \times Q$

$$\begin{cases} \rho(\partial_t(\mathbf{u}_h + \mathbf{u}'), (\mathbf{w}_h + \mathbf{w}'))_\Omega + \rho((\mathbf{u}_h + \mathbf{u}') \cdot \nabla(\mathbf{u}_h + \mathbf{u}'), (\mathbf{w}_h + \mathbf{w}'))_\Omega \\ \quad + (2\mu \boldsymbol{\varepsilon}(\mathbf{u}_h + \mathbf{u}') : \boldsymbol{\varepsilon}(\mathbf{w}_h + \mathbf{w}'))_\Omega - ((p_h + p'), \nabla \cdot (\mathbf{w}_h + \mathbf{w}'))_\Omega = (\mathbf{f}, (\mathbf{w}_h + \mathbf{w}'))_\Omega + (\mathbf{h}, (\mathbf{w}_h + \mathbf{w}'))_{\Gamma_h} \\ (\nabla \cdot (\mathbf{u}_h + \mathbf{u}'), (q_h + q'))_\Omega = 0 \end{cases} \quad (16)$$

As shown previously, these equations can be split into two sub-problems by separating the two scales. Integrating by parts within each element, we obtain the so-called coarse-scale problem

$$\begin{cases} \rho(\partial_t(\mathbf{u}_h + \mathbf{u}'), \mathbf{w}_h)_\Omega + \rho((\mathbf{u}_h + \mathbf{u}') \cdot \nabla(\mathbf{u}_h + \mathbf{u}'), \mathbf{w}_h)_\Omega + (2\mu \boldsymbol{\varepsilon}(\mathbf{u}_h) : \boldsymbol{\varepsilon}(\mathbf{w}_h))_\Omega \\ \quad - ((p_h + p'), \nabla \cdot \mathbf{w}_h)_\Omega = (\mathbf{f}, \mathbf{w}_h)_\Omega + (\mathbf{h}, \mathbf{w}_h)_{\Gamma_h} \quad \forall \mathbf{w}_h \in V_{h,0} \\ (\nabla \cdot (\mathbf{u}_h + \mathbf{u}'), q_h)_\Omega = 0 \quad \forall q_h \in Q_h \end{cases} \quad (17)$$

and the fine-scale problem

$$\begin{cases} \rho(\partial_t(\mathbf{u}_h + \mathbf{u}'), \mathbf{w}')_K + \rho((\mathbf{u}_h + \mathbf{u}') \cdot \nabla(\mathbf{u}_h + \mathbf{u}'), \mathbf{w}')_K + (2\mu\varepsilon(\mathbf{u}') : \varepsilon(\mathbf{w}'))_K \\ - ((p_h + p'), \nabla \cdot \mathbf{w}')_\Omega = (\mathbf{f}, \mathbf{w}')_\Omega + (\mathbf{h}, \mathbf{w}')_{\Gamma_h} \quad \forall \mathbf{w}' \in V'_0 \\ (\nabla \cdot (\mathbf{u}_h + \mathbf{u}'), q')_\Omega = 0 \quad \forall q' \in Q' \end{cases} \quad (18)$$

To derive our stabilized formulation, we first solve the fine scale problem, defined on the sum of element interiors and written in terms of the time-dependent large-scale variables. Then we substitute the fine-scale solution back into the coarse problem (17), thereby *eliminating the explicit appearance of the fine-scale while still modelling their effects*. At this stage, three important remarks and assumptions have to be made:

- (i) by considering the small scale velocity as bubble functions vanishing on the boundaries of the element, terms involving integrals over the element interior boundaries will be neglected [15]
- (ii) we neglect the second derivatives of the weighting function in the momentum residuals of (18)
- (iii) as the fine-scale space is assumed to be H^1 -orthogonal to the finite element space, the crossed viscous terms vanish in (17) and (18) [11];
- (iv) for the sake of clarity, only Dirichlet boundary conditions are considered, generalization to other types of boundary conditions being straightforward.

3.3. The fine scale sub-problem

Rearranging the terms of Eq. (18) leads to:

$$\begin{cases} \rho(\partial_t \mathbf{u}', \mathbf{w}')_\Omega + \rho((\mathbf{u}_h + \mathbf{u}') \cdot \nabla \mathbf{u}', \mathbf{w}')_\Omega + (2\mu\varepsilon(\mathbf{u}') : \varepsilon(\mathbf{w}'))_\Omega + (\nabla p', \mathbf{w}')_\Omega = (\mathcal{R}_M, \mathbf{w}')_\Omega \quad \forall \mathbf{w}' \in V'_0 \\ (\nabla \cdot \mathbf{u}', q')_\Omega = (\mathcal{R}_C, q')_\Omega \quad \forall q' \in Q' \end{cases} \quad (19)$$

with \mathcal{R}_M and \mathcal{R}_C the momentum and continuity residuals, respectively:

$$\begin{aligned} \mathcal{R}_M &= \mathbf{f} - \rho \partial_t \mathbf{u}_h - \rho(\mathbf{u}_h + \mathbf{u}') \cdot \nabla \mathbf{u}_h - \nabla p_h \\ \mathcal{R}_C &= -\nabla \cdot \mathbf{u}_h \end{aligned} \quad (20)$$

Here, some assumptions have to be made in order to deal with the time-dependency and the nonlinearity of the momentum equation of the subscale system (19):

- (i) the subscales are not tracked in time, therefore, quasi-static subscales are considered here (see [35] for a justification of this choice); however, the subscale equation remains quasi time-dependent since it is driven by the large-scale time-dependent residual; (for time-tracking of subscales, see [23])
- (ii) the convective velocity of the nonlinear term may be approximated using only large-scale part so that $(\mathbf{u}_h + \mathbf{u}') \cdot \nabla(\mathbf{u}_h + \mathbf{u}') \approx \mathbf{u}_h \cdot \nabla(\mathbf{u}_h + \mathbf{u}')$.

Consequently, the fine-scale problem reduces to the following:

$$\begin{cases} \rho(\mathbf{u}_h \cdot \nabla \mathbf{u}', \mathbf{w}')_\Omega + (2\mu\varepsilon(\mathbf{u}') : \varepsilon(\mathbf{w}'))_\Omega + (\nabla p', \mathbf{w}')_\Omega = (\mathcal{R}_M, \mathbf{w}')_\Omega \quad \forall \mathbf{w}' \in V'_0 \\ (\nabla \cdot \mathbf{u}', q')_\Omega = (\mathcal{R}_C, q')_\Omega \quad \forall q' \in Q' \end{cases} \quad (21)$$

With regard to the work of [36], two important extensions needed for simulating flows at high Reynolds number can be identified. The first one consists in considering the advection terms in Eq. (21) and the second one is that the small-scale pressure is included. These two extensions are essential for simulating high convection-dominated flows. Indeed, it is known, from the works of Wall et al. [37], Tezduyar and Osawa [38], Hughes and Wells [39] that considering the small-scale pressure as an additional variable enables to complete the continuity condition on the small-scale level. It provides additional stability especially when increasing Reynolds number. However, solving the small-scale equation for both the velocity and the pressure is somewhat complicated. Franca and co-workers [5,6] proposed a separation technique of the small-scale unknowns. They replaced the small-scale continuity equation by the small-scale pressure Poisson equation (PPE). Since only the effect of the small-scale pressure Poisson equation on the large-scale equation must be retained, Franca and Oliveira [40] showed that this equation can be approximately solved by way of an additional term in the fashion of a stabilizing term as follows:

$$p' \approx \tau_C \mathcal{R}_C \quad (22)$$

In this work, we adopt the definition proposed by Codina in [19] for the stabilizing coefficient:

$$\tau_C = \left(\left(\frac{\mu}{\rho} \right)^2 + \left(\frac{c_2}{c_1} \frac{\|\mathbf{u}\|_K}{h} \right)^2 \right)^{1/2} \quad (23)$$

where c_1 and c_2 are two constants independent from h , h being the characteristic length of the element. Once this stabilizing coefficient τ_C has been defined, expression (22) can be inserted into the large scale Eq. (17). Then, it remains to deal with the

small scale momentum equation. Codina has shown in [19] that the small scale velocity is exclusively driven by the residual of the large scale momentum equation and not by the residual of the continuity equation. Consequently, in order to eliminate the effects of the small scale pressure in the small scale momentum equation, we impose $p' = 0$.

Now, it remains to solve the small-scale momentum equation. Following Masud and Khurram [30] and without loss of generality, the fine scale fields can be expanded using bubble functions on individual elements:

$$\mathbf{u}' = \sum_{K \in \mathcal{T}_h} \mathbf{u}'_K b_K \quad \text{and} \quad \mathbf{w}' = \sum_{K \in \mathcal{T}_h} \mathbf{w}'_K b_K \quad (24)$$

where b_K represents the bubble shape functions, \mathbf{u}'_K denotes the vector of coefficients for the fine scale velocity field and \mathbf{w}'_K represents the coefficients for the fine scale weighting function.

Inserting expressions (24) into the fine scale momentum Eq. (21) yields:

$$\sum_{K \in \mathcal{T}_h} \rho(\mathbf{u}_h \cdot \nabla b_K \mathbf{u}'_K, b_K \mathbf{w}'_K)_K + (2\mu \boldsymbol{\epsilon}(b_K \mathbf{u}'_K) : \boldsymbol{\epsilon}(b_K \mathbf{w}'_K))_K = \sum_{K \in \mathcal{T}_h} (\mathcal{R}_M, b_K \mathbf{w}'_K)_K \quad (25)$$

Since the bubble functions vanish on element boundaries, the previous expression simplifies into:

$$\rho(\mathbf{u}_h \cdot \nabla b_K \mathbf{u}'_K, b_K \mathbf{w}'_K)_K + (2\mu \boldsymbol{\epsilon}(b_K \mathbf{u}'_K) : \boldsymbol{\epsilon}(b_K \mathbf{w}'_K))_K = (\mathcal{R}_M, b_K \mathbf{w}'_K)_K \quad \forall K \in \mathcal{T}_h \quad (26)$$

Taking the constant vector of coefficients \mathbf{u}'_K and \mathbf{w}'_K out of the integral and exploiting arbitrariness of \mathbf{w}'_K , one gets:

$$\mathbf{u}'_K = \frac{1}{\rho(\mathbf{u}_h \cdot \nabla b_K, b_K)_K + (2\mu \boldsymbol{\epsilon}(b_K) : \boldsymbol{\epsilon}(b_K))_K} \cdot (\mathcal{R}_M, b_K)_K \quad \forall K \in \mathcal{T}_h \quad (27)$$

Assuming that the large scale momentum residual \mathcal{R}_M is constant for linear tetrahedral elements, the fine scale velocity on each element K can read:

$$\mathbf{u}'|_K = \tau_K \mathcal{R}_M \quad \forall K \in \mathcal{T}_h \quad (28)$$

where τ_K is the stabilization parameter which has been naturally obtained after the resolution of the fine scale sub-problem:

$$\tau_K = \frac{b_K \int_K b_K d\Omega}{\rho(\mathbf{u}_h \cdot \nabla b_K, b_K)_K + (2\mu \boldsymbol{\epsilon}(b_K) : \boldsymbol{\epsilon}(b_K))_K} \quad \forall K \in \mathcal{T}_h \quad (29)$$

The effect of the bubble is now condensed in this element parameter. Obviously, the choice of the bubble functions affects the value of the stability parameter. In expression (29), both convection and viscous regime are represented. However, using the same bubble function for the trial function and the weighting function leads to the cancellation of the convection term. Indeed, under the assumption that \mathbf{u}_h is piecewise constant, the choice of the Mini-element yields:

$$(\mathbf{u}_h \cdot \nabla b_K, b_K)_K = 0 \quad \forall K \in \mathcal{T}_h \quad (30)$$

As pointed out in [9], a way to recover the convection term is to resort to upwind bubbles. Such a choice enables to reproduce naturally the coefficient of the SUPG stabilization method. This issue has been also highlighted by Masud et al. in [30], they propose the use of different-order interpolation functions for the trial and the weighting functions in the skew part of (29). In order to extract the structure of the stability parameter τ_K , we employ a combination of standard bubble shape function b_K and upwind shape functions b_K^u in the fine scale field \mathbf{w}' :

$$\mathbf{w}'|_K = \mathbf{w}'_K b_K^* = \mathbf{w}'_K (b_K + b_K^u) \quad (31)$$

Introducing the modified \mathbf{w}' into (27) leads to the modified form of the stabilization parameter τ_K :

$$\tau_K = \frac{b_K \int_K b_K^* d\Omega}{\rho(\mathbf{u}_h \cdot \nabla b_K, b_K^u)_K + (2\mu \boldsymbol{\epsilon}(b_K) : \boldsymbol{\epsilon}(b_K))_K} \quad \forall K \in \mathcal{T}_h \quad (32)$$

As we use linear interpolations, the second derivatives vanish, consequently the upwind part drops out directly in the viscous term. Note also that from (30), only the upwind terms remains in the convection term. And thus, the stable formulation is maintained and consistent for the Stokes problem.

3.4. The coarse scale sub-problem

Let us consider the coarse scale problem of the expression (17) including the assumptions made for the fine scale fields:

$$\begin{cases} \rho(\partial_t \mathbf{u}_h, \mathbf{w}_h)_\Omega + (\rho \mathbf{u}_h \cdot \nabla \mathbf{u}_h, \mathbf{w}_h)_\Omega + (\rho \mathbf{u}_h \cdot \nabla \mathbf{u}', \mathbf{w}_h)_\Omega + (2\mu \boldsymbol{\epsilon}(\mathbf{u}_h) : \boldsymbol{\epsilon}(\mathbf{w}_h))_\Omega - (p_h, \nabla \cdot \mathbf{w}_h)_\Omega - (p', \nabla \cdot \mathbf{w}_h)_\Omega = (\mathbf{f}, \mathbf{w}_h)_\Omega \quad \forall \mathbf{w}_h \in V_{h,0} \\ \{(\nabla \cdot \mathbf{u}_h, q_h)_\Omega + (\nabla \cdot \mathbf{u}', q_h)_\Omega = 0 \quad \forall q_h \in Q_h \end{cases} \quad (33)$$

Applying integration by parts to the third term in the first equation of (33) and to the second term in the second equation, then substituting the expressions of both the fine-scale pressure (22) and the fine-scale velocity (28), we get:

$$\begin{cases} \rho(\partial_t \mathbf{u}_h + \mathbf{u}_h \cdot \nabla \mathbf{u}_h, \mathbf{w}_h)_\Omega + (\rho \mathbf{u}_h \cdot \nabla \mathbf{u}_h, \mathbf{w}_h)_\Omega - \sum_{K \in T_h} (\tau_K \mathcal{R}_M, \rho \mathbf{u}_h \nabla \mathbf{w}_h)_K + (2\mu \boldsymbol{\varepsilon}(\mathbf{u}_h) : \boldsymbol{\varepsilon}(\mathbf{w}_h))_\Omega - (p_h, \nabla \cdot \mathbf{w}_h)_\Omega + \sum_{K \in T_h} (\tau_C \mathcal{R}_C, \nabla \cdot \mathbf{w}_h)_K = (\mathbf{f}, \mathbf{w}_h)_\Omega \quad \forall \mathbf{w}_h \in V_{h,0} \\ (\nabla \cdot \mathbf{u}_h, q_h)_\Omega - \sum_{K \in T_h} (\tau_K \mathcal{R}_M, \nabla q_h)_K = 0 \quad \forall q_h \in Q_h \end{cases} \quad (34)$$

Finally, substituting the residual of the momentum equation and expanding all the additional terms, we obtain a modified coarse scale equation expressed solely in terms of coarse scale functions. The new modified problem for linear tetrahedral elements can now be decomposed into four main term: the first one is the Galerkin contribution, the second and the third terms take into account the influence of the fine-scale velocity on the finite element components and the last term models the influence of the fine-scale pressure onto the large-scale problem:

$$\begin{aligned} & \underbrace{\rho(\partial_t \mathbf{u}_h + \mathbf{u}_h \cdot \nabla \mathbf{u}_h, \mathbf{w}_h)_\Omega + (2\mu \boldsymbol{\varepsilon}(\mathbf{u}_h) : \boldsymbol{\varepsilon}(\mathbf{w}_h))_\Omega - (p_h, \nabla \cdot \mathbf{w}_h)_\Omega + (\nabla \cdot \mathbf{u}_h, q_h)_\Omega - (\mathbf{f}, \mathbf{w}_h)_\Omega}_{\text{Galerkin terms}} \\ & + \underbrace{\sum_{K \in T_h} \tau_K (\rho(\partial_t \mathbf{u}_h + \mathbf{u}_h \cdot \nabla \mathbf{u}_h) + \nabla p_h - \mathbf{f}, \rho \mathbf{u}_h \nabla \mathbf{w}_h)_K}_{\text{Upwind stabilization terms}} + \underbrace{\sum_{K \in T_h} \tau_K (\rho(\partial_t \mathbf{u}_h + \mathbf{u}_h \cdot \nabla \mathbf{u}_h) + \nabla p_h - \mathbf{f}, \nabla q_h)_K}_{\text{Pressure stabilization terms}} \\ & + \underbrace{\sum_{K \in T_h} (\tau_C \nabla \cdot \mathbf{u}_h, \nabla \cdot \mathbf{w}_h)_K = 0}_{\text{grad-div stabilization term}} = 0 \quad \forall \mathbf{w}_h \in V_{h,0}, \quad \forall q_h \in Q_h \end{aligned} \quad (35)$$

When compared with the standard Galerkin method (15), the proposed stable formulation involves additional integrals that are evaluated element wise. These additional terms, obtained by replacing the approximated \mathbf{u}' and p' into the large-scale equation, represent the effects of the sub-grid scales and they are introduced in a consistent way to the Galerkin formulation. All of these terms enable to overcome the instability of the classical formulation arising in convection dominated flows and to satisfy the inf-sup condition for the velocity and pressure interpolations. Moreover, and with regard to the work of [30], an additional stabilizing term is added last in Eq. (35). It is simply the result of considering the small-scale pressure, which provides additional stability at high Reynolds number [41] and is essential for simulating high convection-dominated flows.

For sake of simplicity in the notation and for a better representation of all the additional terms in Eq. (35), the condensation procedure of the small-scale into the large scale is masked under these stabilizing parameters.

3.5. Time advancing

A general theta-scheme was used and implemented for the time discretization. But for sake of simplicity in the notation and for illustration purposes, we used in the following an implicit backward-Euler time-integration scheme ($\theta = 1$). Therefore, the weak form of the implicit scheme for the coarse scale momentum equation including the small scale pressure simplification reads:

$$\begin{aligned} & \rho \left(\frac{\mathbf{u}_h^{n+1} - \mathbf{u}_h^n}{\Delta t}, \mathbf{w}_h \right)_\Omega + (\rho \mathbf{u}_h \cdot \nabla \mathbf{u}_h, \mathbf{w}_h)_\Omega^{n+1} + (\rho \mathbf{u}_h \cdot \nabla \mathbf{u}', \mathbf{w}_h)_\Omega^{n+1} + (2\mu \boldsymbol{\varepsilon}(\mathbf{u}_h^{n+1}) : \boldsymbol{\varepsilon}(\mathbf{w}_h))_\Omega - (p_h^{n+1}, \nabla \cdot \mathbf{w}_h)_\Omega \\ & + (\tau_C \nabla \cdot \mathbf{u}_h^{n+1}, \nabla \cdot \mathbf{w}_h)_\Omega = (\mathbf{f}^n, \mathbf{w}_h)_\Omega \end{aligned} \quad (36)$$

where the exponent n denotes the current time iteration while the exponent $(n+1)$ represents the next time level we want to compute. The resulting implicit scheme (36) is obviously nonlinear because of the nonlinear nature of the convective terms. In order to address this issue, we resort to a classical Newton–Raphson linearization procedure. The implicit Newton–Raphson iterative scheme reads:

$$\begin{aligned} & \rho \left(\frac{\mathbf{u}_h^{n,i+1} - \mathbf{u}_h^n}{\Delta t}, \mathbf{w}_h \right)_\Omega + (\rho \mathbf{u}_h \cdot \nabla \mathbf{u}_h, \mathbf{w}_h)_\Omega^{n,i+1} + (\rho \mathbf{u}_h \cdot \nabla \mathbf{u}', \mathbf{w}_h)_\Omega^{n,i+1} + (2\mu \boldsymbol{\varepsilon}(\mathbf{u}_h^{n,i+1}) : \boldsymbol{\varepsilon}(\mathbf{w}_h))_\Omega - (p_h^{n,i+1}, \nabla \cdot \mathbf{w}_h)_\Omega \\ & + (\tau_C \nabla \cdot \mathbf{u}_h^{n,i+1}, \nabla \cdot \mathbf{w}_h)_\Omega = (\mathbf{f}^n, \mathbf{w}_h)_\Omega \end{aligned} \quad (37)$$

where the exponent $(n, i+1)$ denotes the $(i+1)$ th iteration of the Newton–Raphson procedure which uses as initial guess the solution at time level n . The linearization of the convective terms consists in keeping only first-order terms at the $(i+1)$ th Newton iteration as follows:

$$\begin{aligned} (\mathbf{u}_h \cdot \nabla \mathbf{u}_h)^{n,i+1} &= \left(\mathbf{u}_h^{n,i} + (\mathbf{u}_h^{n,i+1} - \mathbf{u}_h^{n,i}) \right) \cdot \nabla \left(\mathbf{u}_h^{n,i} + (\mathbf{u}_h^{n,i+1} - \mathbf{u}_h^{n,i}) \right) \\ &= \mathbf{u}_h^{n,i} \cdot \nabla \mathbf{u}_h^{n,i+1} + \mathbf{u}_h^{n,i+1} \cdot \nabla \mathbf{u}_h^{n,i} - \mathbf{u}_h^{n,i} \cdot \nabla \mathbf{u}_h^{n,i} + \left(\mathbf{u}_h^{n,i+1} - \mathbf{u}_h^{n,i} \right) \cdot \nabla \left(\mathbf{u}_h^{n,i+1} - \mathbf{u}_h^{n,i} \right) \\ &\approx \mathbf{u}_h^{n,i} \cdot \nabla \mathbf{u}_h^{n,i+1} + \mathbf{u}_h^{n,i+1} \cdot \nabla \mathbf{u}_h^{n,i} - \mathbf{u}_h^{n,i} \cdot \nabla \mathbf{u}_h^{n,i} \end{aligned} \quad (38)$$

with $\mathbf{u}_h^{n,i}$ the value of the velocity at the previous Newton iteration. Since we are using quasi-static bubble functions, the third term of Eq. (37) reduces to:

$$(\mathbf{u}_h \cdot \nabla \mathbf{u}')^{n,i+1} \approx \mathbf{u}_h^{n,i} \cdot \nabla \mathbf{u}'^{n,i+1} \quad (39)$$

The complete linearized Newton–Raphson scheme finally reads:

$$\begin{aligned} & \rho \left(\frac{\mathbf{u}_h^{n,i+1}}{\Delta t} + \mathbf{u}_h^{n,i} \cdot \nabla \mathbf{u}_h^{n,i+1} + \mathbf{u}_h^{n,i+1} \cdot \nabla \mathbf{u}_h^{n,i}, \mathbf{w}_h \right)_\Omega + \left(\rho \mathbf{u}_h^{n,i} \cdot \nabla \mathbf{u}'^{n,i+1}, \mathbf{w}_h \right)_\Omega + \left(2\mu \boldsymbol{\epsilon}(\mathbf{u}_h^{n,i+1}) : \boldsymbol{\epsilon}(\mathbf{w}_h) \right)_\Omega \\ & - \left(\mathbf{p}_h^{n,i+1}, \nabla \cdot \mathbf{w}_h \right)_\Omega + (\tau_c \nabla \cdot \mathbf{u}_h^{n,i+1}, \nabla \cdot \mathbf{w}_h)_\Omega = \left(\mathbf{f}^n + \rho \frac{\mathbf{u}_h^n}{\Delta t} + \mathbf{u}_h^{n,i} \cdot \nabla \mathbf{u}_h^{n,i}, \mathbf{w}_h \right)_\Omega \end{aligned} \quad (40)$$

3.6. Matrix formulation of the problem

When applied to both the coarse scale system and the fine scale system, the previous scheme gives rise to a linear system that remains to be solved. This system can be put naturally under the following matrix form:

$$\begin{bmatrix} A_{ww} & {}^t A_{wb} & {}^t A_{wq} \\ A_{wb} & A_{bb} & {}^t A_{bq} \\ A_{wq} & A_{bq} & 0 \end{bmatrix} \begin{bmatrix} \mathbf{u}_h \\ \mathbf{u}' \\ p_h \end{bmatrix} = \begin{bmatrix} B_w \\ B_b \\ B_q \end{bmatrix} \quad (41)$$

where

$$\begin{aligned} A_{ww}(\mathbf{u}_h) &= \rho \left(\frac{\mathbf{u}_h^{n,i+1}}{\Delta t} + \mathbf{u}_h^{n,i} \cdot \nabla \mathbf{u}_h^{n,i+1} + \mathbf{u}_h^{n,i+1} \cdot \nabla \mathbf{u}_h^{n,i}, \mathbf{w}_h \right)_\Omega + \left(2\mu \boldsymbol{\epsilon}(\mathbf{u}_h^{n,i+1}) : \boldsymbol{\epsilon}(\mathbf{w}_h) \right)_\Omega + \left(\tau_c \nabla \cdot \mathbf{u}_h^{n,i+1}, \nabla \cdot \mathbf{w}_h \right)_\Omega \\ A_{bb}(\mathbf{u}') &= \rho \left(\mathbf{u}_h^{n,i} \cdot \nabla \mathbf{u}'^{n,i+1}, \mathbf{w}' \right)_\Omega + (2\mu \boldsymbol{\epsilon}(\mathbf{u}'^{n,i+1}) : \boldsymbol{\epsilon}(\mathbf{w}'))_\Omega \\ A_{wb}(\mathbf{u}_h) &= \rho \left(\frac{\mathbf{u}_h^{n,i+1}}{\Delta t} + \mathbf{u}_h^{n,i} \cdot \nabla \mathbf{u}_h^{n,i+1} + \mathbf{u}_h^{n,i+1} \cdot \nabla \mathbf{u}_h^{n,i}, \mathbf{w}' \right)_\Omega \\ A_{wq}(\mathbf{u}_h) &= - \left(\nabla \cdot \mathbf{u}_h^{n,i+1}, q_h \right)_\Omega \\ A_{bq}(\mathbf{u}') &= - \left(\nabla \cdot \mathbf{u}'^{n,i+1}, q_h \right)_\Omega \end{aligned} \quad (42)$$

and

$$\begin{aligned} B_w &= \left(\mathbf{f}^n + \rho \frac{\mathbf{u}_h^n}{\Delta t} + \mathbf{u}_h^{n,i} \cdot \nabla \mathbf{u}_h^{n,i}, \mathbf{w}_h \right)_\Omega \\ B_w &= \left(\mathbf{f}^n + \rho \frac{\mathbf{u}_h^n}{\Delta t} + \mathbf{u}_h^{n,i} \cdot \nabla \mathbf{u}_h^{n,i}, \mathbf{w}' \right)_\Omega \\ B_b &= \left(\mathbf{f}^n + \rho \frac{\mathbf{u}_h^n}{\Delta t} + \mathbf{u}_h^{n,i} \cdot \nabla \mathbf{u}_h^{n,i}, \mathbf{w}' \right)_\Omega \\ B_q &= 0 \end{aligned} \quad (43)$$

One can notice that, in the present case of the quasi-static bubble assumption, the following simplification holds:

$${}^t A_{wb}(\mathbf{u}') = \rho \left(\mathbf{u}_h^{n,i} \cdot \nabla \mathbf{u}'^{n,i+1}, \mathbf{w}' \right)_\Omega \quad (44)$$

The static condensation process, previously detailed, which consists in solving the second line involving \mathbf{u}' and inserting the solution into the first and third lines of system (41) results into the condensed matrix scheme for large-scale unknowns \mathbf{u}_h and p_h that reads:

$$\begin{bmatrix} \tilde{A}_{ww} & {}^t \tilde{A}_{wq} \\ \tilde{A}_{wq} & \tilde{A}_{qq} \end{bmatrix} \begin{bmatrix} \mathbf{u}_h \\ p_h \end{bmatrix} = \begin{bmatrix} \tilde{B}_w \\ \tilde{B}_q \end{bmatrix} \quad (45)$$

with

$$\begin{aligned} \tilde{A}_{ww} &= A_{ww} - {}^t A_{wb} A_{bb}^{-1} A_{wb} \quad {}^t \tilde{A}_{wq} = {}^t A_{wb} A_{bb}^{-1} {}^t A_{bq} \\ \tilde{A}_{wq} &= A_{wq} - A_{bq} A_{bb}^{-1} A_{wb} \quad \tilde{A}_{qq} = -A_{bq} A_{bb}^{-1} {}^t A_{bq} \\ \tilde{B}_w &= B_w - {}^t A_{wb} A_{bb}^{-1} B_b \quad \tilde{B}_q = -A_{bq} A_{bb}^{-1} B_b \end{aligned} \quad (46)$$

Taking into account locally the influence of unresolved fine scales upon the resolved large scales has introduced new stabilizing terms and modified the components of all the matrices while the effect of the fine-scale pressure has been added directly to the first matrix by a stabilizing term. This matrix formulation can be put in relation with the classic expression (35) as follows:

- (i) the modified terms \tilde{A}_{ww} and \tilde{A}_{wq} incorporate the upwind stabilization terms provided by ${}^t A_{wb} A_{bb}^{-1} A_{wb}$ and $A_{bq} A_{bb}^{-1} A_{wb}$;
- (ii) similarly, the modified operators ${}^t \tilde{A}_{wq}$ and \tilde{A}_{qq} contain the pressure stabilization terms ${}^t A_{wb} A_{bb}^{-1 t} A_{bq}$ and $A_{bq} A_{bb}^{-1 t} A_{bq}$;
- (iii) eventually, the right hand side components have been modified to ensure consistency by means of ${}^t A_{wb} A_{bb}^{-1} B_b$ and $A_{bq} A_{bb}^{-1} B_b$.

4. Numerical examples

In order to assess the main characteristics of this formulation and to test its feasibility in the context of high-performance computing, both 2D and 3D examples are analyzed. They were chosen to cover different flow situations at high Reynolds number, and to deal with time-dependent flow problems as well.

First we consider the 2D lid-driven cavity for different Reynolds numbers. This is a standard benchmark problem. Comparisons with the literature using different methods are presented for Reynolds up to only 20,000. While using similar approach, authors in [30,31] presented results up to only 10,000. In the following section, we continue to test the performance of the developed method for Reynolds numbers of 33,000 and 50,000. In the second part, we investigate the proposed approach on full three-dimensional instationary flow situations in the cavity up to Reynolds number 12,000. Comparisons with the experimental data are presented. We conclude in the third part with the famous backward-facing step example. This example join three attractive features: first, the Reynolds number is chosen to be equal 42,000, second, we used a heterogeneous mesh where both isotropic and anisotropic refinement are applied, and finally, new quantitative results are provided.

Note that these computations shown in the following qualify this formulation as a tool to be used within the domain of simulation of real flows. That is especially due to the fact that it does not require any turbulence-type modelling and, thus, can be applied to any region of the domain, regardless of the flow regime. All the stabilisation terms introduced to the classical formulation plays an important role. It allows then simulation of flows at different Reynolds number, in particularly, the simulation of a turbulent flow in 3D at Reynolds number equal to 12,000 without the need of any turbulence modelling, averaging quantities, or additional eddy viscosities.

All the numerical implementations as well as the simulations were carried out by using the C++ CimLib finite element library (see [42,43]).

4.1. Driven flow cavity problem (2D)

We begin to numerically solve the classical lid-driven flow problem. This test has been widely used as a benchmark for numerical methods and has been analyzed by a number of authors [44–47]. The problem description, boundary conditions and the corresponding meshes are shown in Fig. 1. Dirichlet boundary conditions prescribe on the upper boundary at $y = 1$, and elsewhere on. The source term is identical to zero. The viscosity is adjusted in order to obtain Reynolds number of 1,000, 5,000, 10,000, 20,000, 33,000 and 50,000. Zero pressure is prescribed at the lower left corner.

Two meshes of linear finite elements have been used in the calculations. The coarse one is made of 64×64 elements, refined near the walls of the cavity. The fine mesh is made of 180×180 elements. All numerical experiments are compared to the very known references of Ghia et al. [44] and Erturk et al. [48]. The authors in [44] applied a second-order accurate finite difference method using a fine grid of 257×257 while in [48] the 2D steady incompressible Navier–Stokes equations was solved using a very efficient finite difference numerical method (fourth order compact formulation) on a very fine grid of

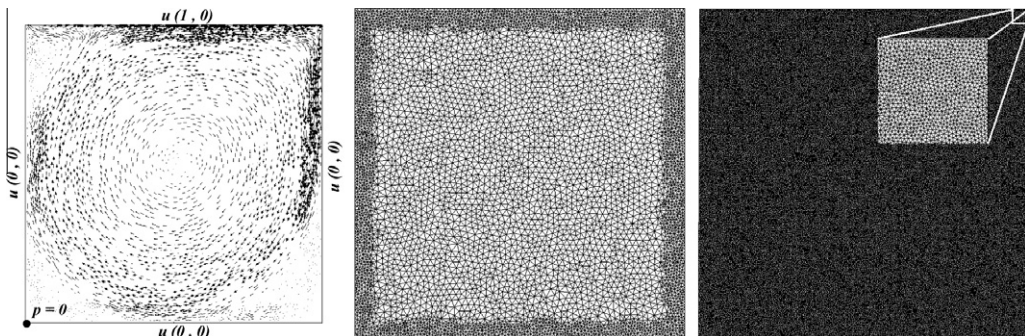


Fig. 1. Problem settings: boundary conditions (left), coarse mesh (center), fine mesh (right).

601×601 . We consider that the steady state is reached when the normalized velocity deviations within one step are lower than a chosen tolerance of 10^{-6} . Recall that the main interest is to compare the performance of the implemented scheme described in the previous section and the behaviour of the solution for high Reynolds number flows. Therefore, a first set

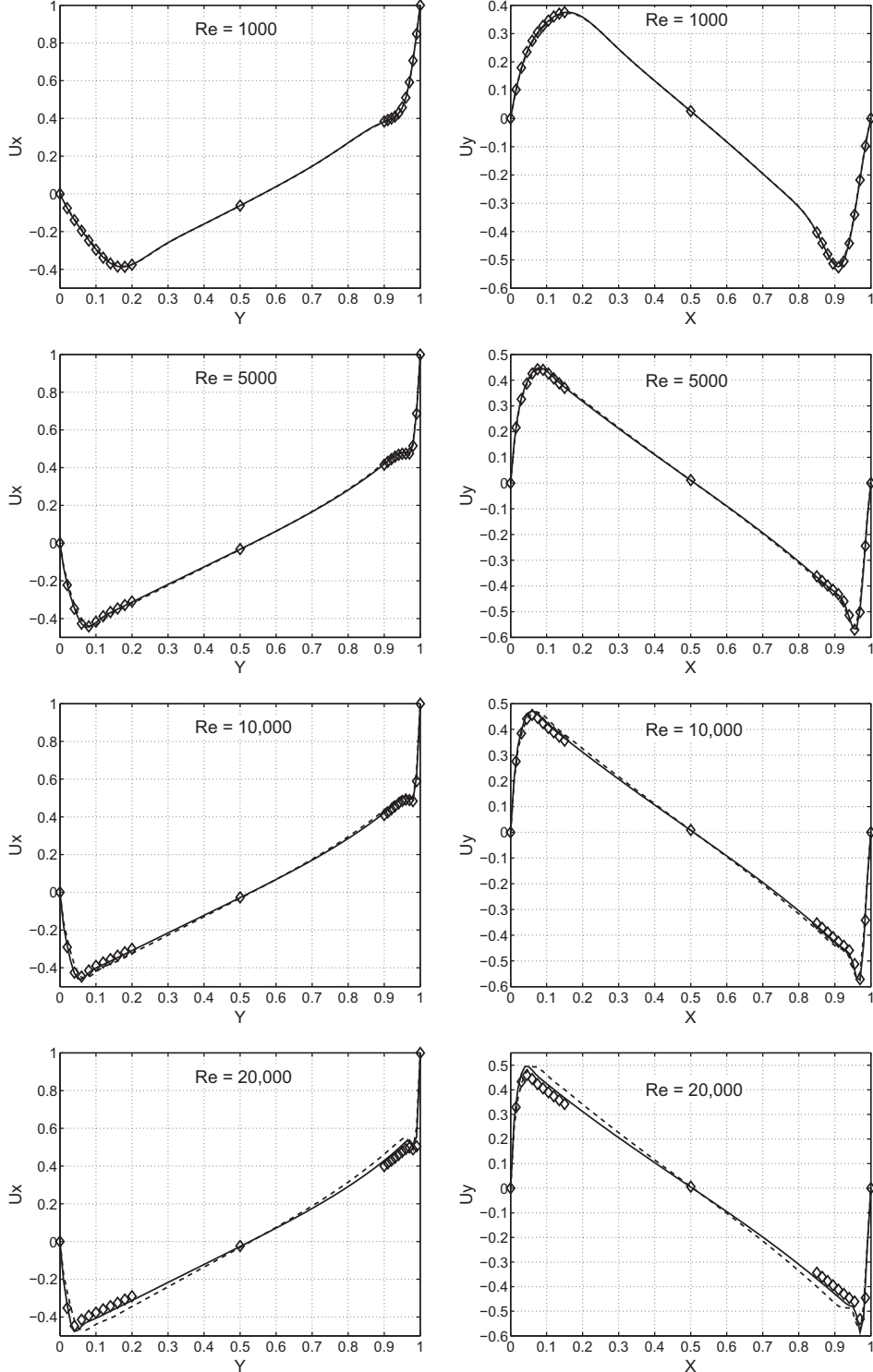


Fig. 2. Left: velocity profile for u_x along $x = 0.5$. Right: velocity profile for u_y along $y = 0.5$. The dashed and solid lines denote the coarse and fine meshes respectively while the symbols represent the reference [48].

of numerical experiments has been performed. The velocity profiles for u_x and u_y along $x = 0.5$ and $y = 0.5$ respectively are shown in Fig. 2. Comparing these results with the given reference, one can clearly see the agreement of the solutions in particularly when the Reynolds number increases. Hence, we conclude that the presence of the pressure subscale and the convection terms in the small-scale problem renders an accurate solution even on the coarse mesh. Some other interesting quantities than plotting the velocity profiles are available in the literature. In [31], the authors have studied and analyzed the pressure and the vortex formation and comparisons were made using several numerical methods for different Reynolds number. In the following, we will use these results and we will get a closer look on the pressure isolines for Reynolds number 10,000 and compared our results to the given reference. Table 1 and Fig. 3 show a very good agreement of the pressure solution with the given reference. As in [36], we proceed our comparisons by investigating the location of the respective vortex centres. Fig. 4 shows the computed flow fields in terms of the velocity magnitude and the corresponding streamlines.

As expected, using the fine mesh 180×180 the solutions exhibit additional counter-rotating vortices in or near the cavity corners as Re increases. It is known that this problem involves a primary vortex, while for higher Reynolds numbers secondary vortices appear in the corners of the domain. As the Reynolds number increases, the location of the centres of these vortices change, secondary vortex has the tendency to break on two new vortices and consequently their number increases (see Figs. 4 and 5). The effect of the Reynolds number on the genesis of new vortices inside the cavity is presented in Table 2. Fig. 6 highlights by order of appearance the location of these expected vortices. The location of the centres of these vortices together with corresponding values from references solutions are summarized in Tables 3 and 4. Qualitatively and quantitatively, the results are similar to reference solutions and a good agreement is observed, although the mesh used here is coarser than the one used in the reference. We have used as reference [44] for number of Reynolds less than 10,000, and [48] for $Re = 20,000$. To our knowledge, results for Reynolds number 33,000 and 50,000 using linear stabilized finite elements methods are considered very rare. We notice a very interesting periodic behaviour of these computations which will be subject of further investigations.

The velocity profiles for u_x and u_y along $x = 0.5$ and $y = 0.5$ respectively for Reynolds number 33,000 and 50,000 are shown in Fig. 7. Another set of numerical experiments was conducted in order to study the convergence of the implemented formulation. We performed a mesh sensitivity study to validate the capability of the method. Therefore, five different unstructured grids were used for these comparisons with a mesh of 16×16 , 32×32 , 64×64 , 80×80 and 125×125 elements respectively. The Reynolds number is chosen to be equal to 5,000. We compute the error of the velocity solution using the L^2 -norm for all mesh sizes h as follows:

$$\text{err}(h) = \left(\sum_{x,y} (u_{\text{ref}}^i - u_k^i)^2 \right)^{1/2} \quad \forall h \quad (47)$$

Results are compared to [48] obtained by employing a high-order accurate finite difference method on a 601×601 mesh. The approximation error is plotted in Fig. 8 and shows the expected improvement in the results. The velocity profiles

Table 1

Minimum and maximum values of the pressure for various numerical methods for the coarse mesh (64×64) and for $Re = 10,000$.

	Present work	USFEM [18]	Two-level method [5]	Three-level method [31]
p_{\min}	-0.1319	-0.0975	-0.0730	-0.0904
p_{\max}	0.9142	0.8774	1.0465	1.1278

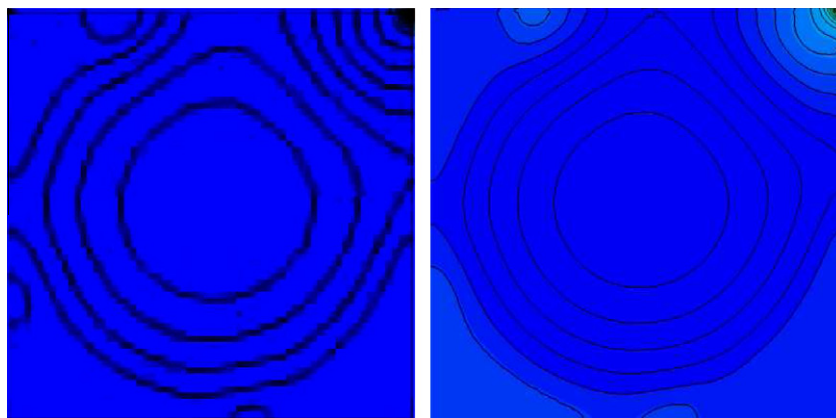


Fig. 3. Pressure isolines on colored pressure distribution. Left: two-level method [31]. Right: present work.

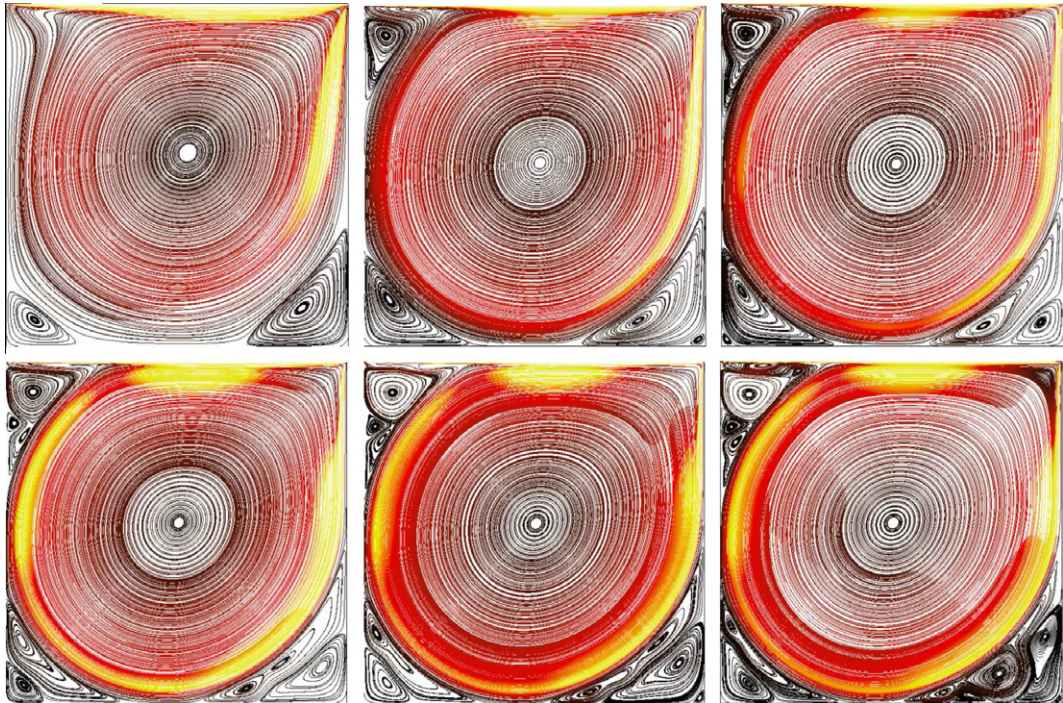


Fig. 4. Streamline on colored velocity distribution from top-left to bottom-right: $Re = 1000, 5000, 10000, 20000, 33000$ and 50000 with 180×180 mesh.

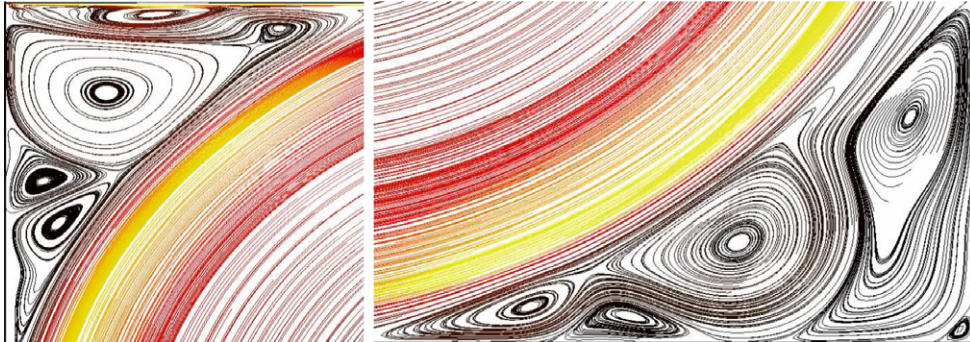


Fig. 5. A magnified view of various secondary vortices near the cavity corners for $Re = 50000$.

Table 2
Number of resolved vortices in function of the Reynolds number.

Reynolds	Vortices
1,000	3
5,000	5
10,000	6
20,000	8
30,000	10
50,000	13

employing different grid resolutions together with the reference solution are shown in Fig. 9. Note that the present method converges rather rapidly to the given benchmark solution.

We conclude this numerical example by examining the computer demands. The number of time steps needed to reach the steady state with $\Delta t = 0.1$ s, as well as the required CPU time, are reported in Fig. 10. Within each time step only a single iteration is performed. As expected, the required CPU time increases with the Reynolds number. This is due to the fact that the physical time is longer to yield the solution; the ratio (CPU time/real time) remaining quite constant in all cases.

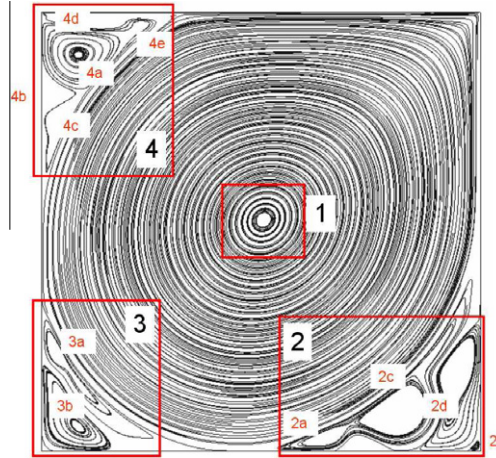


Fig. 6. Location of the resolved vortices in order of appearance.

Table 3

Location of vortex centres (coordinate x , coordinate y) for the two first zones (V_1, V_2) compared to data from [44,48].

Reynolds values		10,000	20,000	33,000	50,000
V_{1a}	Current	(0.5110, 0.5310)	(0.5080, 0.5280)	(0.506, 0.527)	(0.506, 0.526)
	Reference	(0.5117, 0.5330)	(0.5100, 0.5267)	–	–
V_{2a}	Current	(0.7670, 0.0594)	(0.7060, 0.0416)	(0.667, 0.0350)	(0.654, 0.0309)
	Reference	(0.7656, 0.0586)	(0.7267, 0.0450)	–	–
V_{2b}	Current	(0.9330, 0.0689)	(0.9290, 0.1060)	(0.926, 0.119)	(0.99, 0.0112)
	Reference	(0.9336, 0.0625)	(0.9300, 0.1033)	–	–
V_{2c}	Current		(0.808, 0.115)	(0.863, 0.178)	(0.816, 0.0857)
	Reference	–	–	–	–
V_{2d}	Current			(0.986, 0.017)	(0.95, 0.194)
	Reference	–	–	–	–
V_{2e}	Current				(0.732, 0.0218)
	Reference	–	–	–	–

Table 4

Location of vortex centres (coordinate x , coordinate y) for the two last zones (V_3, V_4) compared to data from [44,48].

Reynolds values		10,000	20,000	33,000	50,000
V_{3a}	Current	(0.0589, 0.1600)	(0.0489, 0.1820)	(0.0375, 0.206)	(0.0307, 0.226)
	Reference	(0.0586, 0.1641)	(0.0483, 0.1817)	–	–
V_{3b}	Current	(0.0160, 0.0191)	(0.0536, 0.0511)	(0.0692, 0.0602)	(0.0831, 0.0556)
	Reference	(0.0156, 0.0195)	(0.0567, 0.0533)	–	–
V_{4a}	Current	(0.0710, 0.9110)	(0.0802, 0.9120)	(0.0852, 0.911)	(0.0839, 0.908)
	Reference	(0.0703, 0.9141)	(0.0817, 0.9133)	–	–
V_{4b}	Current		(0.0255, 0.82)	(0.0339, 0.811)	(0.0317, 0.809)
	Reference		(0.0233, 0.82)	–	–
V_{4c}	Current		(0.0539, 0.783)	(0.0537, 0.774)	(0.0446, 0.763)
	Reference	–	–	–	–
V_{4d}	Current				(0.126, 0.988)
	Reference			–	–
V_{4e}	Current				(0.228, 0.972)
	Reference			–	–

4.2. Three-dimensional lid-driven cavity flow

In many industrial, environmental and geophysical flows, the 3D lid-driven cavity flow can be seen as an interesting recirculating flow. The flow is confined in a cubic domain with the upper wall moving at a constant speed (see Fig. 11 for de-

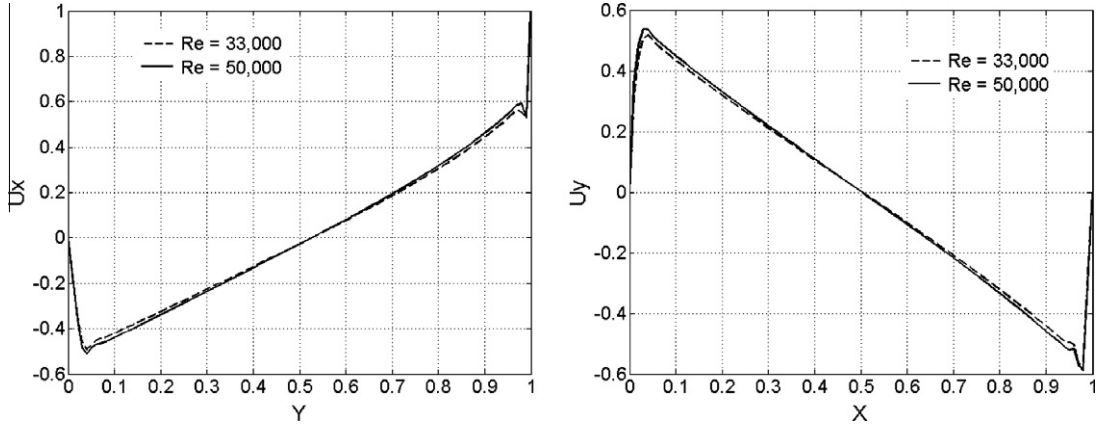


Fig. 7. Velocity profile for u_x along $x = 0.5$ (left) and u_y along $y = 0.5$ (right).

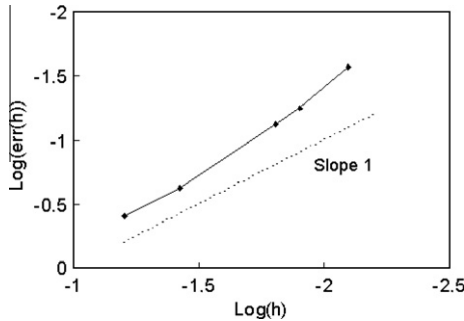


Fig. 8. Evolution of the error in function of the mesh size h .

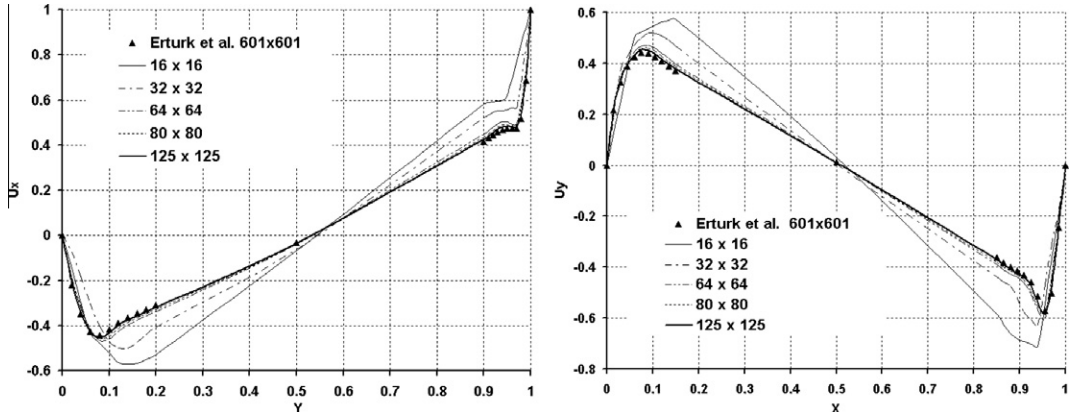


Fig. 9. Velocity profile using different meshes. Left: u_x along $x = 0.5$. Right: u_y along $y = 0.5$.

tails). Although the geometry is simple, complex physical phenomena occurs inside the cubic cavity. Contrary to the 2D case presented in the previous section, new phenomena can be captured with the 3D simulations. The presence of side-walls confining the full flow modifies the flow pattern so that three-dimensional structures that significantly altered the primary flow in the central plane are produced. Recently, the use of three-dimensional numerical simulation becomes a very interesting tool for investigating such physical phenomena in particularly thanks to the increase of technological advances in computer hardware and parallel computing.

A literature review on the 3D problem shows that in fact by examining a plane parallel to the downstream wall, corner eddies were caused at the juncture of the side-walls and the ground while downstream secondary vortices appeared. More-

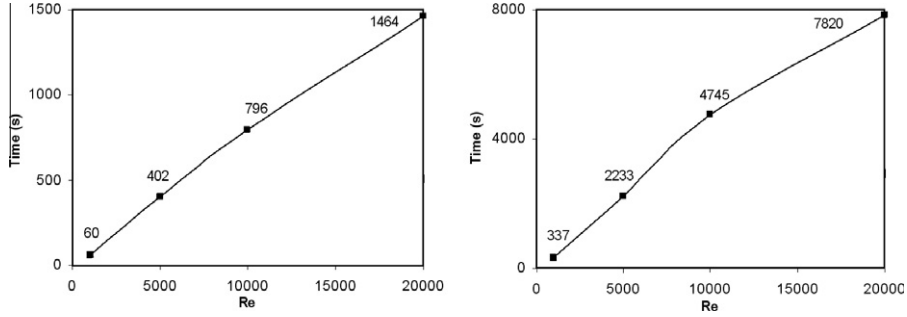


Fig. 10. Required physical time (left) and CPU time (right) to reach the steady state for different Reynolds number.

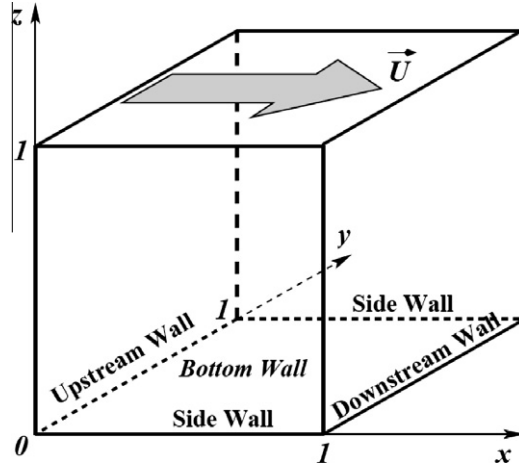


Fig. 11. Sketch of the 3D lid driven cavity problem.

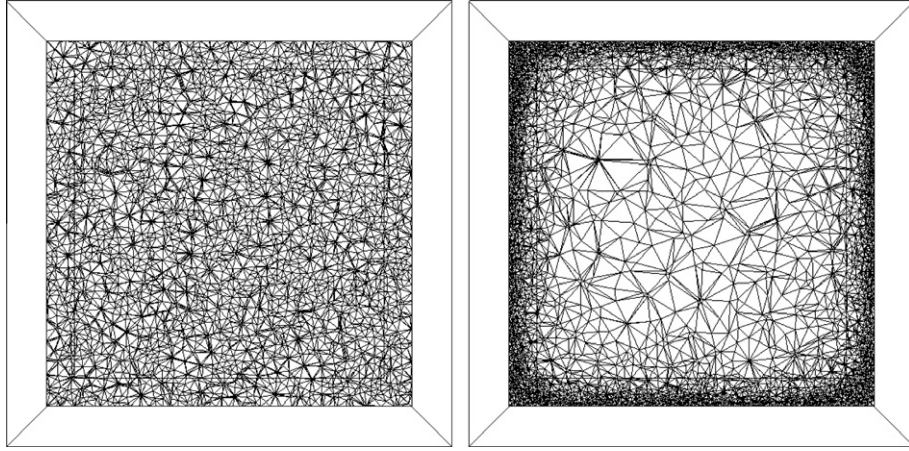


Fig. 12. Heterogeneous isotropic mesh for 3D lid-driven cavity flow.

over, due to centrifugal forces along the downstream, eddy separation surface were found along the span. These vortices are known as Taylor-Görter-like (TGL) vortices in reference to their curvature-induced origins. As shown in the 2D numerical test, the number and location of these vortices were also depending on the Reynolds number. The experimental visualization of these vortices were first accomplished at Stanford University by Koseff et al. [49,50]. The numerical prediction of these vortices has to be credited to the work of Freitas et al. [51,52]. It was mentioned that not only corner vortices in the vicinity of the vertical end-walls were observed but also locally spreading TGL vortices. For instance, eight pairs of TGL vortices were

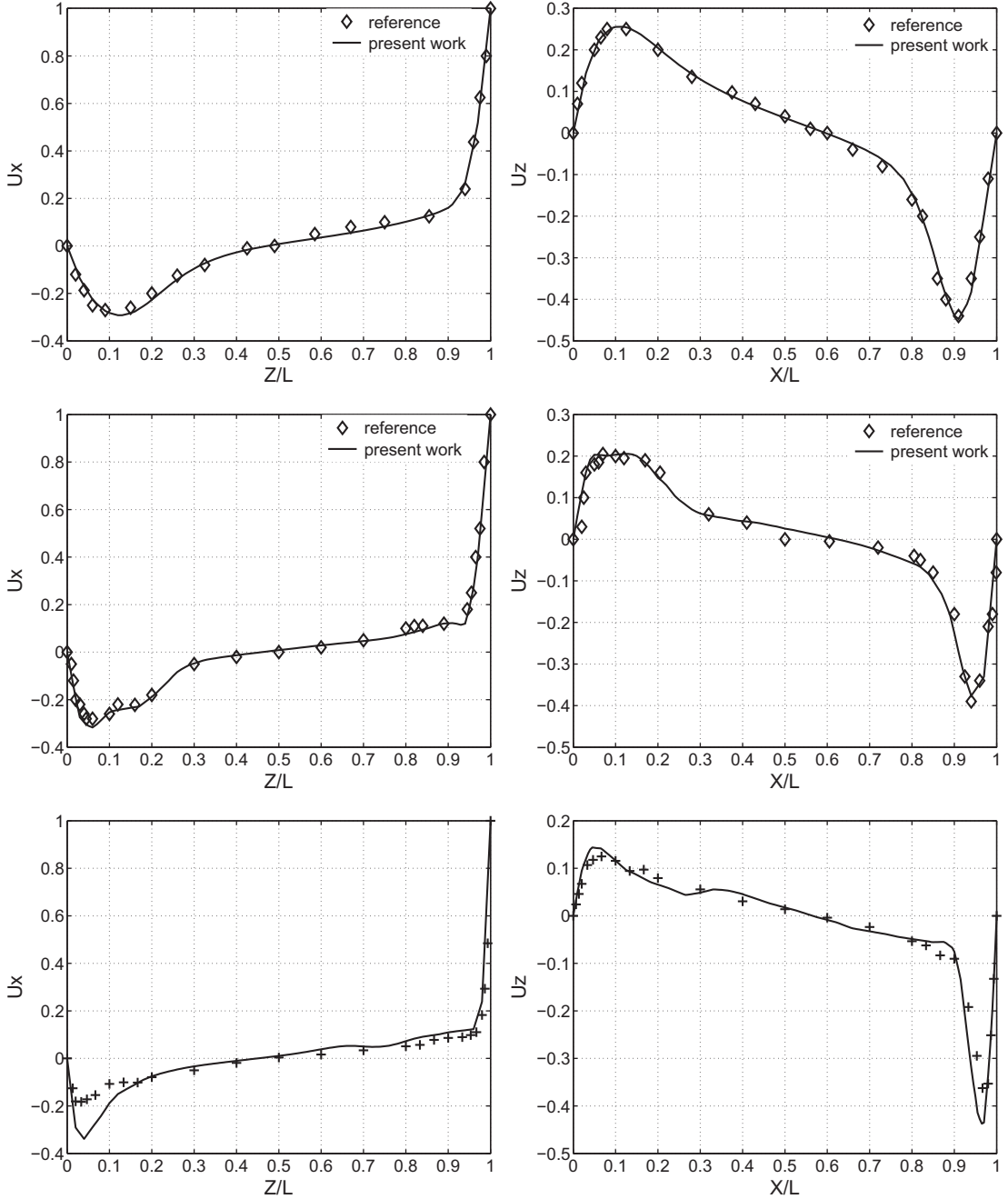


Fig. 13. Comparison of velocity profiles in the mid-plane $y = 0.5$ with reference data (symbols) from [53] for $Re = 1,000$ (top), [54] for $Re = 3,200$ (middle) and [55] for $Re = 12,000$ (bottom). Left: mean value of velocity in the x -direction. Right: mean value of velocity in the z -direction.

observed for $Re \approx 3,000$. For higher Reynolds numbers, regular unsteadiness is no longer sustained and thus evolved into turbulence.

From a numerical point of view, it is worth noticing that most of the computations were made using structured grids due to the simplicity of the geometry in order to capture the flow phenomenon accurately. Consequently, few calculations were performed using unstructured grids. Here, in this work, two unstructured tetrahedral grids were employed to simulate the lid-driven cavity flow: the first, referred to as the coarse mesh, consists of 36,282 nodes and 192,080 linear tetrahedral elements, and the second, referred to as the fine mesh, consists of 238,580 nodes and 1,229,089 linear tetrahedral elements with grid clustering near the six cavity walls. These grids are displayed in Fig. 12. Aiming at comparing our results with the given reference, the two different meshes employed here are formed by approximately the same number of elements

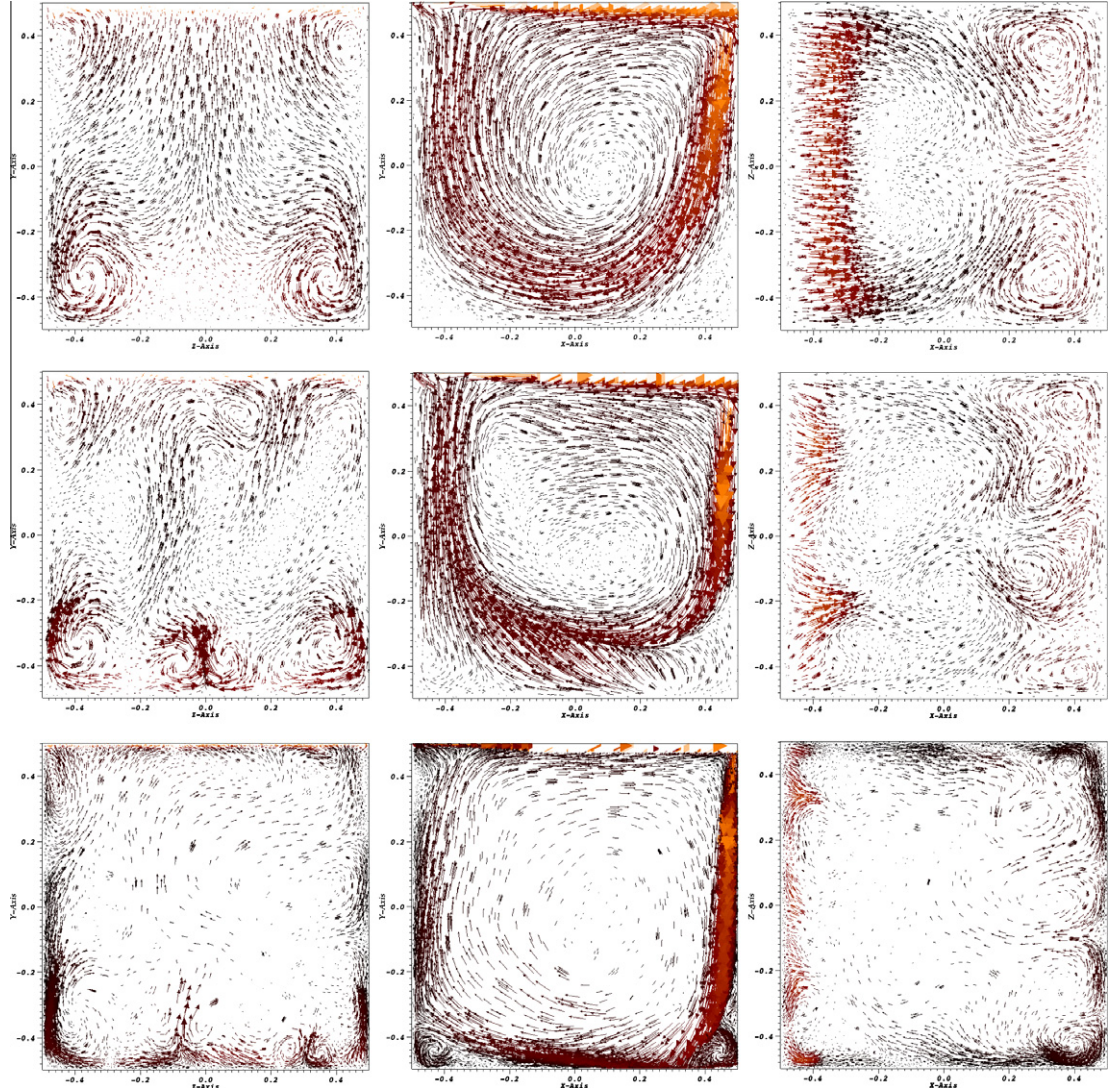


Fig. 14. Comparison of velocity vectors for different Reynolds number: $Re = 1,000$ (top); $Re = 3,200$ (middle) and $Re = 12,000$ (bottom) along different planes: plane $y - z$ (left); plane $x - y$ (middle); plane $z - x$ (right).

(see [56] for the coarse mesh and [57] for the fine mesh). In order to reveal the Taylor-Görtler structures, we investigate the flow vectors, after 2,000 time units, on the three middle planes $x = 0.5$, $y = 0.5$ and $z = 0.5$.

The initial velocity in the flow is set to zero everywhere except on the lid surface. The viscosity is adjusted to obtain the desired Reynolds number. The computational results for $Re = 1,000$, $Re = 3,200$ and $Re = 12,000$ are compared to the results from Tang et al. [53], Zang et al. [54] and Prasad and Koseff [55] respectively. The fluid motion is generated by the top lid that moves in the x -direction with a constant velocity $U_0 = 1$ m/s. However, in order to avoid discontinuity in Dirichlet boundary conditions, we resort to the following velocity profile in the manner of [57] or [58].

$$U_x = U_0 \left(1 - \left(\frac{2x}{L} \right)^{18} \right)^2 \left(1 - \left(\frac{2y}{L} \right)^{18} \right)^2 \quad (48)$$

where L is the size of the cavity. For all the remaining walls, no-slip conditions are applied.

Following the lines in [57] a fixed time step of 0.1 s is employed and 20,000 time steps (2,000 time units) are performed. Since the detailed convergence analysis is not within the goals of this paper, only the velocity profiles in the mid-plane are plotted and compared with the reference solutions. It is worth to mention that for $Re \geq 3,200$, all the experimental and numerical observations reported by Koseff [49,50] and Zang [54], showed that the steady state does not exist but the transient behaviours become periodic. Consequently, a time interval, for which oscillations of the velocity field occur, was identified and statistical studies in this period were carried out in order to obtain the mean velocity profiles. Figs. 13 and 14 show

the velocity profiles of u_x component on the vertical centreline and u_z component on the horizontal centreline of the symmetry plane $z = 0.5$ for $Re = 1,000$, $Re = 3,200$ and $Re = 12,000$, respectively. The symbols denote the results of the reference data extracted from their figures. All the velocity profiles are in good agreement with profiles reported by the given references. As mentioned previously, as the flow is unsteady, the instantaneous velocity at the same time step is different from the experimental results. Only the time-averaged velocity profile of fully developed flow is plotted and agrees well with the experimental results. The profile is the average value of 100 dimensionless time units. The differences with the experimental results is most probably due to the fact that the grid is not fine enough to simulate accurately such complex fluid phenomena. However, as a first implementation, the agreement between the present and the experimental results has been considered satisfactory.

At $Re = 1,000$, a primary vortex appearing in the plane $x - y$ is coming with two secondary contra-rotating vortices next to the downstream and bottom walls as shown in planes $y - z$ and $z - x$. Moreover, two additional vortices can be observed in the top corners of plane $y - z$. The steadiness of the flow is clearly highlighted by its symmetry. These results are in perfect agreement with those of Yang et al. [59] and Wong and Baker [60]. When the Reynolds number increases, the centre of the primary vortex moves toward the centre of the cube in the same way than the two-dimensional lid-driven square cavity. Furthermore, the size of the secondary vortices decreases while their number is rising. The flow loses its symmetry indicating that it becomes unsteady. Although no quantitative measurements were reported in the given references, similar behaviour of the velocity field was reported by [51,61,62].

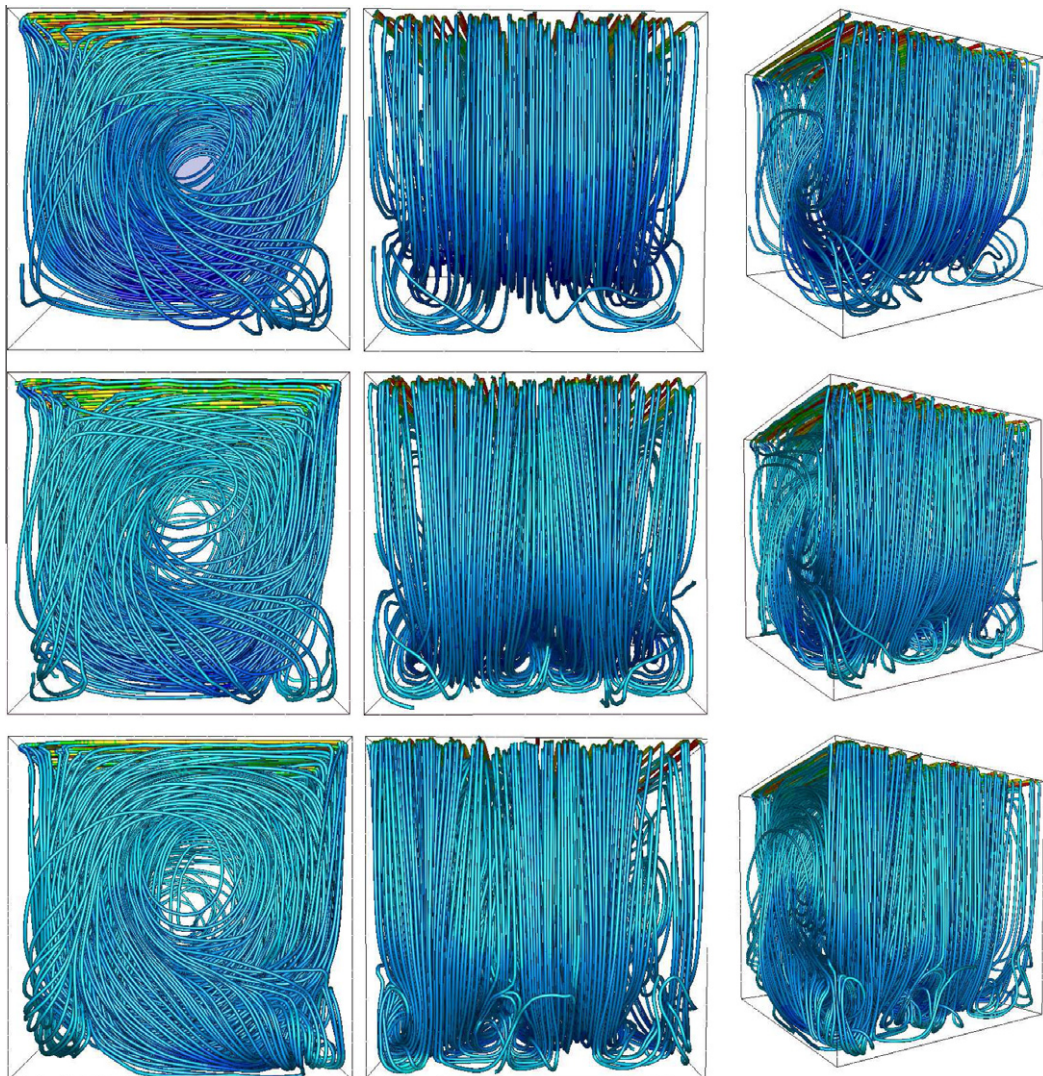


Fig. 15. Comparison of observed streamtraces for different Reynolds number: $Re = 1,000$ (top); $Re = 3,200$ (middle) and $Re = 12,000$ (bottom) on different views: front view (left); side view (middle); oblique view (right).

For high Reynolds number ($Re = 12,000$), the complexity of the flow is clearly highlighted by the streamtraces displayed in Fig. 15. The flow structure is composed by a primary eddy, a downstream secondary eddy, an upstream tertiary eddy and a corner eddy. It is noticed that the route of moving particles reveals a qualitatively new feature for higher Reynolds number. The particle is no longer limited to a single side of the cavity, but instead, it can pass from one side to the other, and back again violating the mirror symmetry. As shown by front view in Fig. 15, the corresponding spiraling path explores the full width of the cavity.

4.3. The flow over a backward-facing step

In this last section, the flow in a backward facing step is analyzed. This problem has been the subject of a detailed experimental study by [63] and has served for many years as a benchmark for turbulent flow solvers. Despite the simplicity of its geometry and boundary condition, it has characteristics of a very complex flow with layers separation, reattachment and recirculation which occurs in many practical engineering applications. The computational domain is presented in Fig. 16. Solid walls are at the top, bottom and the frontal face of the channel. Non-slip boundary conditions were applied at those walls while a parabolic profile U_y [64] is imposed at the channel entrance. The different experimental parameters used in the simulation are taken from [65]: the step height is $H = 5.08$ cm, the maximum mean velocity at the centre of the canal is such that $U^0 = 11.562$ m/s, the kinetic laminar viscosity (air) is taken as $\nu = 1.4 \times 10^{-5}$ m²/s, the density is equal to $\rho = 1.208$ kg/m³, the obtained Reynolds number is $Re = 42,000$ and, eventually, the time step is such that $\Delta t = 0.0002$ s. At the outlet, the normal stress and the velocity U_y are set to zero. The 2D computational mesh consists of approximately 18,973 nodes and 37,246 triangular elements and is depicted in Fig. 17. It contains two isotropic parts with different mesh sizes (see Table 5). Additionally and as shown, local anisotropic mesh refinement was employed in the vicinity of the walls and in the shear layer behind the step. The aspect ratio in these regions is equal to 4.5. The main objective of this numerical

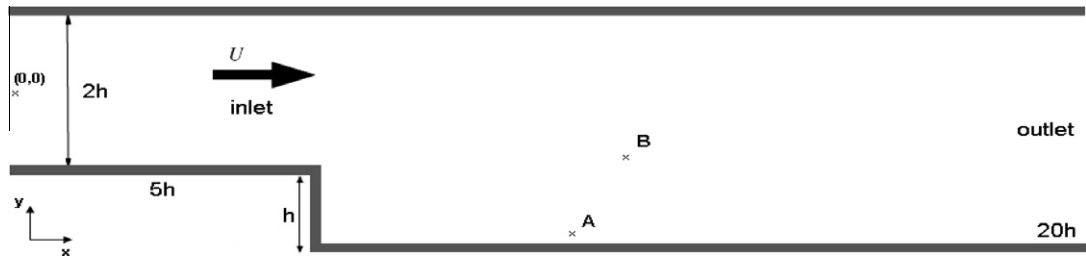


Fig. 16. Geometry and boundary condition of the problem.

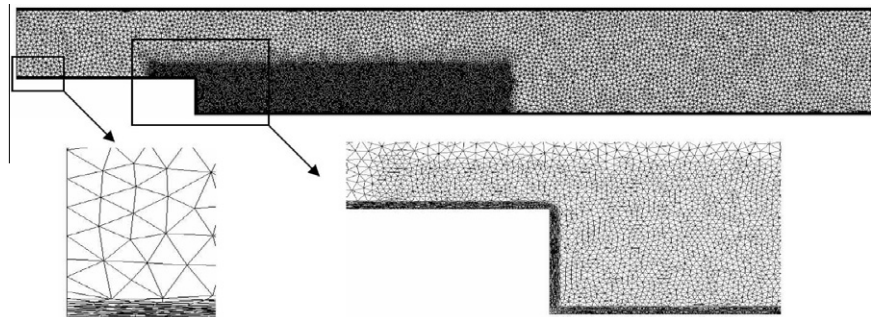


Fig. 17. Anisotropic mesh refinement near the walls.

Table 5

Details of the anisotropy of the meshes.

	Mesh size I	Mesh size II	Aspect ratio
Average value	0.0025	0.007	4.5

example is to test the performance of the implemented method on heterogeneous meshes where both isotropic and anisotropic refinements are applied. Some additional quantitative evaluations will be reported as well.

The majority of published work on separated-reattached flow in this geometry deals with either laminar flows using direct simulation or turbulent flows using suitable turbulence models. However, comparatively little direct numerical simulations (DNS) with high Reynolds number are published (e.g. the work and results by Le et al. [66]). Note that at high Reynolds number, the fully transient flow comes from the upstream of the step, forming a thin boundary layer along the side

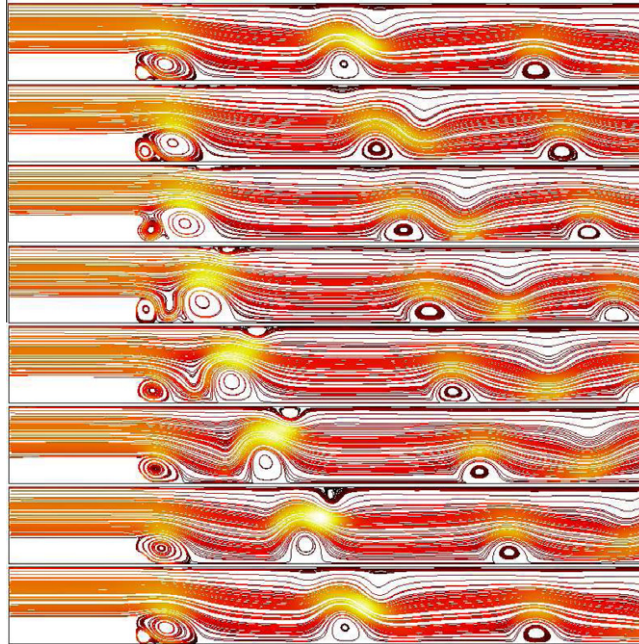


Fig. 18. Periodic evolution of streamlines from $t = 3.04$ s to $t = 3.11$ s.

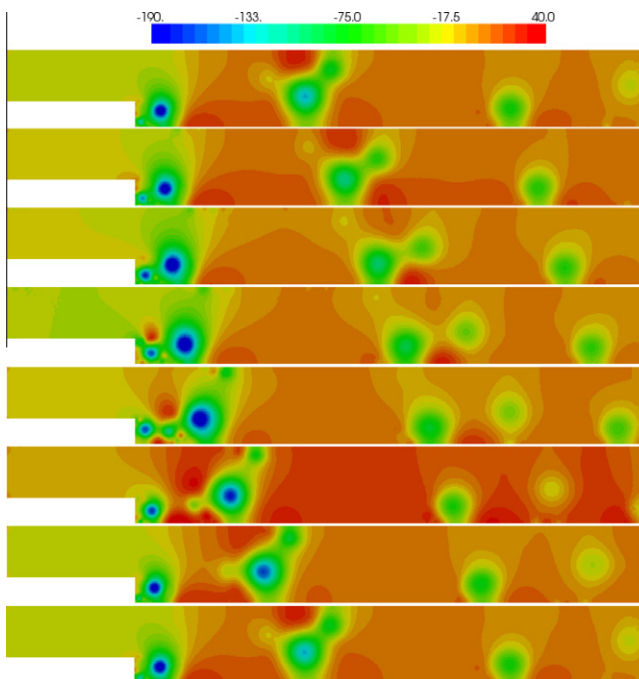


Fig. 19. Periodic evolution of the pressure from $t = 3.04$ s to $t = 3.11$ s.

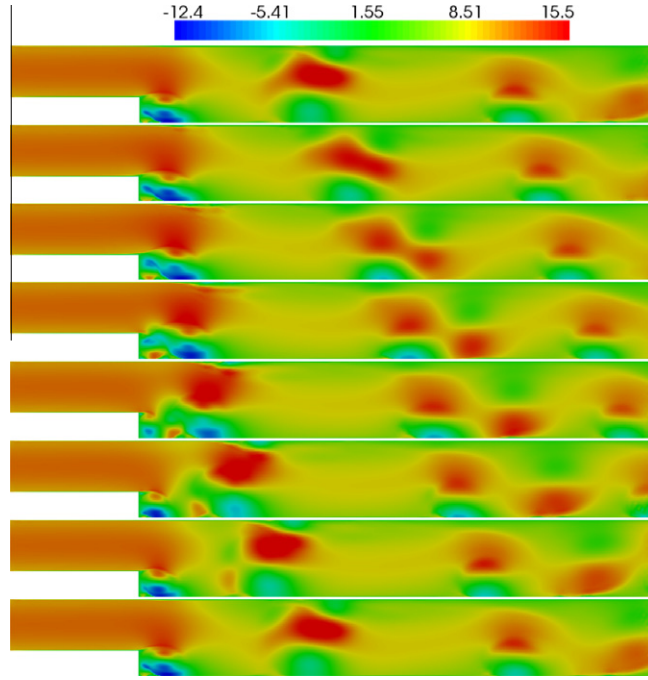


Fig. 20. Periodic evolution of the streamwise velocity from $t = 3.04$ s to $t = 3.11$ s.

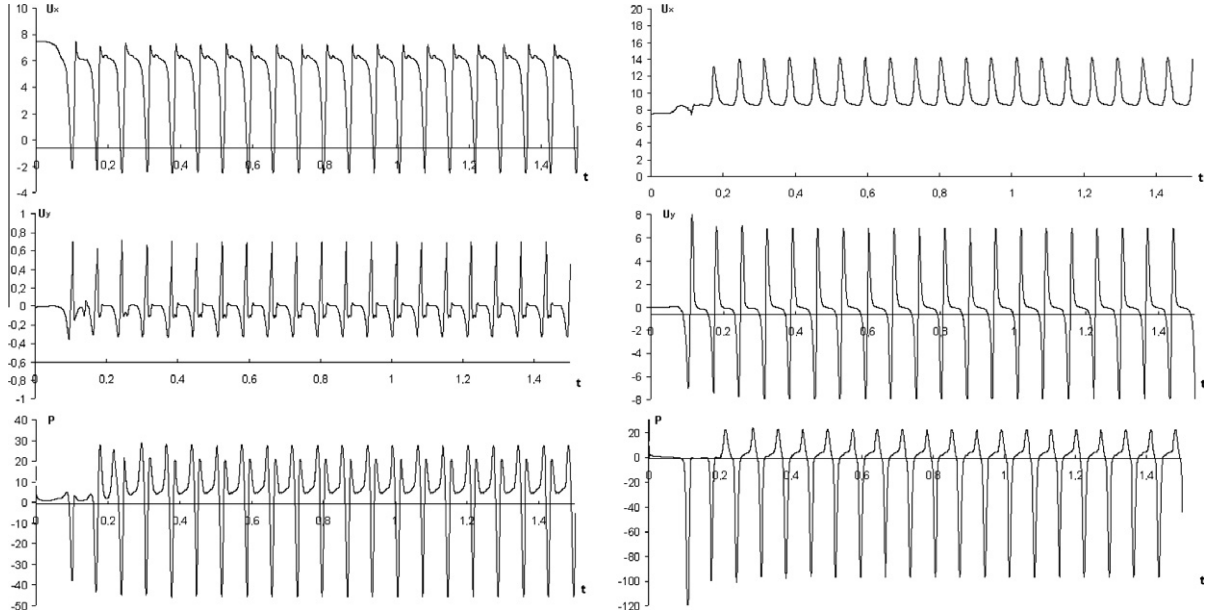


Fig. 21. Periodic evolution of the velocity and the pressure at point A and B.

wall. The variation in the development of the streamlines, the pressure and the velocity is shown in Figs. 18–20 respectively starting from an arbitrary reference time. The shear layer rolls up forming a large-scale structure behind the step. As the largescale structure grows, the reattachment location moves downstream, than suddenly decreases indicating a detachment of the turbulent large-scale from the step. This movement of turbulent vortices is also described by the pressure field. From Fig. 19, one can clearly see that the low-pressure regions have been shown to correspond to the centres of coherent vortices. In two-dimensional simulations at high Reynolds numbers, the authors in [67,68] have indicated the presence of oscillatory flow behaviour in the solution. This is clearly shown in the basic characteristics of the flow given by these plots. Moreover, the velocity components and the pressure contours appear to be qualitatively appropriate without any non-physical oscil-

lations in particular around the corner. The velocity and pressure fluctuations as a function of time at two locations A and B; the first near the reattachment zone $6h$ ($x = 0.5588, y = -0.098806$) and the second in the middle of the channel ($x = 0.631103, y = -0.030696$) are plotted in Fig. 21. Similar oscillatory responses are detected at those points in the flow fields. The Strouhal number corresponding to the dominant frequency is roughly $St = f h/U^0 = 0.06$, with a period $T = 17h/U^0$. These values are in close agreement with previous experimental and numerical deductions given by [66].

Finally, we can conclude that from all these illustrations, there is no presence of any spurious oscillations in the solutions, in particularly for the pressure. The implemented method has proved to work well on such heterogeneous meshes with highly stretched elements near the walls.

5. Conclusion

In this paper, an unstructured finite element incompressible Navier–Stokes solver based on the use of the variational multiscale approach has been successfully developed for the study of 2D and 3D unsteady incompressible flows at high Reynolds numbers. The decomposition of both unknowns, the velocity and the pressure fields, into coarse and fine-scales is considered. By substituting the modelled fine-scale velocity and pressure fields in the coarse-scale problem, additional stabilization terms were added to the standard Galerkin formulation. These terms enhance the stability and accuracy of the classical formulation.

Results obtained via this method have been compared and analyzed with existing data and are in very good agreement. In particular, both the lid-driven cavity problem at Reynolds number up to 20,000 for the 2D case and up to 12,000 for the 3D case were considered. New results using this method were also presented in particularly, the 2D lid-driven cavity with Reynolds number of 33,000 and 50,000, as well as the flow over a backward facing step with Reynolds number equal to 42,000. Taking into account the small-scale velocity part in the convection terms of the small-scale equation is a possible extension of the method.

Acknowledgment

The authors gratefully acknowledge grants from the ADEME, support from CIM Team and the companies involved in the THOST project managed by Science Computer and Consultants (SCC).

References

- [1] H. Yang, T. Chen, Z. Zhu, Numerical study of forced turbulent heat convection in a straight square duct, *International Journal of Heat and Mass Transfer* 52 (2009) 3128–3136.
- [2] H. Yagi, M. Kawahara, Optimal shape determination of a body located in incompressible viscous fluid flow, *Computer Methods in Applied Mechanics and Engineering* 196 (2007) 5084–5091.
- [3] E. Oñate, A. Valls, J. García, Modeling incompressible flows at low and high Reynolds numbers via a finite calculus–finite element approach, *Journal of Computational Physics* 224 (1) (2007) 332–351.
- [4] E. Hachem, Stabilized finite element method for heat transfer and turbulent flows inside industrial furnaces, Ph.D. thesis, Ecole Nationale Supérieure des Mines de Paris, 2009.
- [5] L. Franca, A. Nesliturk, On a two-level finite element method for the incompressible Navier–Stokes equations, *International Journal for Numerical Methods in Engineering* 52 (2001) 433–453.
- [6] A. Nesliturk, Approximating the incompressible Navier–Stokes equations using a two level finite element method, Ph.D. thesis, University of Colorado, 1999.
- [7] D. Arnold, F. Brezzi, M. Fortin, A stable finite element for the Stokes equations, *Calcolo* 23 (4) (1984) 337–344.
- [8] C. Canuto, V. Van Kemenade, Bubble-stabilized spectral methods for the incompressible Navier–Stokes equations, *Computer Methods in Applied Mechanics and Engineering* 135 (1996) 35–61.
- [9] F. Brezzi, A. Russo, Choosing bubbles for advection-diffusion problems, *Mathematical Models and Methods in Applied Sciences* 4 (1994) 571–587.
- [10] A. Russo, Bubble stabilization of finite element methods for linearized incompressible Navier–Stokes equations, *Computer Methods in Applied Mechanics and Engineering* 132 (1996) 335–343.
- [11] F. Brezzi, M. Fortin, Mixed and Hybrid Finite Element Methods, Springer Series in Computational Mathematics, vol. 15, Springer-Verlag, New-York, 1991.
- [12] F. Brezzi, L. Franca, T. Hughes, A. Russo, Stabilization techniques and subgrid scales capturing, in: Conference of the State of the Art in Numerical Analysis, York, England, 1996.
- [13] J. Donea, A. Huerta, Finite Element Methods for Flow Problems, New-York, 2003.
- [14] T. Hughes, Multiscale phenomena: Green's functions, the Dirichlet-to-Neumann formulation, subgrid scale models, bubbles and the origin of stabilized methods, *Computer Methods in Applied Mechanics and Engineering* 127 (1995) 387–401.
- [15] F. Brezzi, L. Franca, T. Hughes, A. Russo, $b = \int g$, *Computer Methods in Applied Mechanics and Engineering* 145 (1997) 329–339.
- [16] T.J.R. Hughes, G. Scovazzi, P.B. Bochev, A. Buffa, A multiscale discontinuous Galerkin method with the computational structure of a continuous Galerkin method, *Computer Methods in Applied Mechanics and Engineering* 195 (19–22) (2006) 2761–2787.
- [17] T. Tezduyar, R. Shih, S. Mittal, S. Ray, Incompressible flow computations with stabilized bilinear and linear equal-order-interpolation velocity–pressure elements, *Computer Methods in Applied Mechanics and Engineering* 95 (1992) 221–242.
- [18] L. Franca, C. Farhat, Bubble functions prompt unusual stabilized finite element methods, *Computer Methods in Applied Mechanics and Engineering* 123 (1995) 229–308.
- [19] R. Codina, Stabilization of incompressibility and convection through orthogonal sub-scales in finite element methods, *Computer Methods in Applied Mechanics and Engineering* 190 (13–14) (2000) 1579–1599.
- [20] R. Codina, Stabilized finite element method for the transient Navier–Stokes equations based on a pressure gradient projection, *Computer Methods in Applied Mechanics and Engineering* 182 (3–4) (2000) 277–300.
- [21] R. Codina, Pressure stability in fractional step finite element methods for incompressible flows, *Journal of Computational Physics* 170 (1) (2001) 112–140.

- [22] R. Codina, J. Principe, Dynamic subscales in the finite element approximation of thermally coupled incompressible flows, *International Journal for Numerical Methods in Fluids* 54 (2007) 707–730.
- [23] R. Codina, J. Principe, O. Guasch, S. Badia, Time dependent subscales in the stabilized finite element approximation of incompressible flow problems, *Computer Methods in Applied Mechanics and Engineering* 196 (21–24) (2007) 2413–2430.
- [24] V. Gravemeier, Scale-separating operators for variational multiscale large eddy simulation of turbulent flows, *Journal of Computational Physics* 212 (2) (2006) 400–435.
- [25] V. Gravemeier, A consistent dynamic localization model for large eddy simulation of turbulent flows based on a variational formulation, *Journal of Computational Physics* 218 (2) (2006) 677–701.
- [26] V. Gravemeier, M.W. Gee, M. Kronbichler, W.A. Wall, An algebraic variational multiscale multigrid method for large eddy simulation of turbulent flow, *Computer Methods in Applied Mechanics and Engineering* 199 (13–16) (2010) 853–864.
- [27] A. Brooks, T. Hughes, Streamline upwind/Petrov–Galerkin formulations for convection dominated flows with particular emphasis on the incompressible Navier–Stokes equations, *Computer Methods in Applied Mechanics and Engineering* 32 (1982) 199–259.
- [28] T.J.R. Hughes, G.R. Feijoo, L. Mazzei, J.N. Quincy, The variational multiscale method a paradigm for computational mechanics, *Computer Methods in Applied Mechanics and Engineering* 166 (1998) 3–24.
- [29] G. Scovazzi, A discourse on Galilean invariance, SUPG stabilization, and the variational multiscale framework, *Computer Methods in Applied Mechanics and Engineering* 196 (4–6) (2007) 1108–1132.
- [30] A. Masud, R.A. Khurram, A multiscale finite element method for the incompressible Navier–Stokes equations, *Computer Methods in Applied Mechanics and Engineering* 195 (2006) 1750–1777.
- [31] V. Gravemeier, W.A. Wall, E. Ramm, A three-level finite element method for the instationary incompressible Navier–Stokes equations, *Computer Methods in Applied Mechanics and Engineering* 193 (15–16) (2004) 1323–1366.
- [32] T.J.R. Hughes, L. Mazzei, K. Jansen, Large eddy simulation and the variational multiscale method, *Computing and Visualization in Science* (2000) 3–47.
- [33] T.J.R. Hughes, A. Oberai, L. Mazzei, Large eddy simulation of turbulent channel flows by the variational multiscale method, *Physics of Fluids* 13 (2001) 1784–1799.
- [34] T.J.R. Hughes, L. Mazzei, A. Oberai, The multiscale formulation of large eddy simulation: decay of homogeneous isotropic turbulence, *Physics of Fluids* 13 (2001) 505511.
- [35] T. Dubois, F. Jauberteau, R. Temam, *Dynamic Multilevel Methods and the Numerical Simulation of Turbulence*, Cambridge University Press, Cambridge, 1999.
- [36] O. Basset, *Simulation numérique d'écoulements multi-fluides sur grille de calcul*, Ph.D. thesis, Ecole Nationale Supérieure des Mines de Paris, 2006.
- [37] W.A. Wall, M. Bischoff, E. Ramm, A deformation dependent stabilization technique, exemplified by EAS elements at large strains, *Computer Methods in Applied Mechanics and Engineering* 188 (4) (2000) 859–871.
- [38] T.E. Tezduyar, Y. Osawa, Finite element stabilization parameters computed from element matrices and vectors, *Computer Methods in Applied Mechanics and Engineering* 190 (3–4) (2000) 411–430.
- [39] T.J.R. Hughes, G.N. Wells, Conservation properties for the Galerkin and stabilised forms of the advection–diffusion and incompressible Navier–Stokes equations, *Computer Methods in Applied Mechanics and Engineering* 194 (9–11) (2005) 1141–1159.
- [40] L.P. Franca, S.P. Oliveira, Pressure bubbles stabilization features in the Stokes problem, *Computer Methods in Applied Mechanics and Engineering* 192 (2003) 1929–1937.
- [41] M.A. Behr, L.P. Franca, T.E. Tezduyar, Stabilized finite element methods for the velocity–pressure–stress formulation of incompressible flows, *Computer Methods in Applied Mechanics and Engineering* 104 (1) (1993) 31–48.
- [42] H. Digonnet, T. Coupez, Object-oriented programming for fast and easy development of parallel applications in forming processes simulation, in: *Computational Fluid and Solid Mechanics 2003*, 2003, pp. 1922–1924.
- [43] Y. Mesri, H. Digonnet, T. Coupez, Advanced parallel computing in material forming with CIMLIB, *European Journal of Computational Mechanics* 18 (7–8) (2009) 669–694.
- [44] U. Ghia, K.N. Ghia, C.T. Shin, High-Re solutions for incompressible flow using the Navier–Stokes equations and a multigrid method, *Journal of Computational Physics* 48 (3) (1982) 387–411.
- [45] R. Schreiber, H.B. Keller, Driven cavity flows by efficient numerical techniques, *Journal of Computational Physics* 49 (1983) 310–333.
- [46] O. Botella, R. Peyret, Benchmark spectral results on the lid-driven cavity flow, *Computers and Fluids* 27 (4) (1998) 421–433.
- [47] M. Sahin, R.G. Owens, A novel fully-implicit finite volume method applied to the lid-driven cavity problem. Part I: high Reynolds number flow calculations, *International Journal for Numerical Methods in Fluids* 42 (2003) 57–77.
- [48] E. Erturk, T.C. Corke, Gokcol, Numerical solutions of 2-D steady incompressible driven cavity flow at high Reynolds numbers, *International Journal for Numerical Methods in Fluids* 48 (7) (2005) 747–774.
- [49] J.R. Koseff, R.L. Street, P.M. Gresho, C.D. Upson, J.A.C. Humphrey, J.W. To, A three-dimensional lid-driven cavity flow: experiment and simulation, in: *Third International Conference on Numerical Methods in Laminar and Turbulent Flow*, Seattle, WA, 1983, pp. 564–581.
- [50] J.R. Koseff, R.L. Street, Visualization studies of a shear driven three-dimensional recirculating flow, *Journal of Fluids Engineering* 106 (1984) 21–29.
- [51] C.J. Freitas, R.L. Street, A.N. Fidikakis, J.R. Koseff, Numerical simulation of three dimensional flow in a cavity, *International Journal for Numerical Methods in Fluids* 5 (1985) 561–575.
- [52] C.J. Freitas, R.L. Street, Non-linear transport phenomena in a complex recirculating flow: a numerical investigation, *International Journal for Numerical Methods in Fluids* 8 (1988) 769–802.
- [53] L.Q. Tang, T. Cheng, T.T.H. Tsang, Transient solutions for three-dimensional lid-driven cavity flows by a least-squares finite element method, *International Journal for Numerical Methods in Fluids* 21 (1995) 413–432.
- [54] Y. Zang, R.L. Street, J.R. Koseff, A dynamic mixed subgrid-scale model and its application to turbulent recirculating flows, *Physics of Fluids* A5 (1993) 3186–3196.
- [55] A.K. Prasad, J.R. Koseff, Reynolds number and end-wall effects on a lid-driven cavity flow, *Physics of Fluids* A1 (1989) 208–218.
- [56] T.L. Popiolek, A.M. Awruch, P.R.F. Teixeira, Finite Element Analysis of Laminar and Turbulent Flows Using LES and Subgrid-Scale Models, *Applied Mathematical Modelling* 30 (2) (2006) 177–199.
- [57] E.F. Lins, R.N. Elias, G.M. Guerra, F.A. Rochinha, A.L. Coutinho, Edge-based finite element implementation of the residual-based variational multiscale method, *International Journal for Numerical Methods in Fluids* 61 (2009) 1–22.
- [58] R. Bouffanais, E. Leriche, M.O. Deville, Large-eddy simulation of the flow in a lid-driven cubical cavity, *Physics of Fluids* 19 (5) (2007) 055108.
- [59] J.Y. Yang, S.C. Yang, Y.N. Chen, C.A. Hsu, Implicit weighted ENO schemes for the three-dimensional incompressible Navier–Stokes equations, *Journal of Computational Physics* 146 (1) (1998) 464–487.
- [60] K.L. Wong, A.J. Baker, A 3D incompressible Navier–Stokes velocity–vorticity weak form finite element algorithm, *International Journal for Numerical Methods in Fluids* 38 (2002) 99–123.
- [61] J.R. Koseff, R.L. Street, The lid-driven cavity flow: a synthesis of qualitative and quantitative observations, *Journal of Fluids Engineering* 106 (1984) 390–398.
- [62] J.R. Koseff, R.L. Street, On end wall effects in a lid-driven cavity flow, *Journal of Fluids Engineering* 106 (1984) 385–389.
- [63] J. Kim, Investigation of separation and reattachment of turbulence shear layer: flow over a backward facing step, Ph.D. thesis, Stanford University, 1978.
- [64] B.E. Launder, D.B. Spalding, The numerical computation of turbulent flows, *Computer Methods in Applied Mechanics and Engineering* 3 (2) (1974) 269–289.

- [65] L. Gaston, Simulation numTrique par TITments finis bidimensionnels du remplissage de moules de fonderie et Ttude expTrimentale sur maquette hydraulique, Ph.D. thesis, Ecole Nationale SupTrieure des Mines de Paris, 1997.
- [66] H. Le, P. Moin, J. Kim, Direct numerical simulation of turbulent flow over a backward-facing step, Journal of Fluid Mechanics 330 (1997) 349–374.
- [67] H. Le, P. Moin, Direct numerical simulation of turbulent flow over a backward-facing step, Report TF-58, Stanford University, 1994.
- [68] W.F. Zhu, X.H. Wang, Large Eddy Simulation of Re's Influence on the Quasi-Periodic Motions of the Turbulent Flow Over a Backward-Facing Step, New Trends in Fluid Mechanics Research ISBN 978-3-540-75994-2 (Springer Berlin Heidelberg), 2009, pp. 131–133.